Tampere University

Karem Lozano Montero

ULTRA-THIN IDE PULSE WAVE SENSOR

Faculty of Information Technology and Communication Sciences
Master of Science Thesis
November 19

ABSTRACT

Karem Lozano Montero: Ultra-thin IDE Pulse Wave Sensor

Master of Science Thesis

Tampere University

Master's Degree Program in Electrical Engineering

November 19

The monitoring of vital signs is used to determine human health status. Healthcare monitoring devices are usually attached to the human skin to obtain information about the human body. However, the main inconvenience of using conventional electronic devices is the mechanical mismatch between the devices and the skin. This issue can lead to measurement errors, and patient comfort can be affected negatively when these devices are used continuously. Therefore, it is needed to develop skin-conformal electronic devices to overcome these drawbacks. This thesis explores the fabrication process of ultrathin interdigitated pulse wave sensors based on the piezoelectric effect. The aim of this research is to demonstrate that printed electronics technologies are an excellent alternative to fabricate low-cost skin-conformal sensors.

First, this thesis explores the theoretical background of piezoelectricity, flexible and ultrathin piezoelectric pressure sensors, and printed electronics technologies. Then, the fabrication process is analyzed. The sensor is fabricated onto a Parylene-C substrate using the piezoelectric polymer P(VDF-TrF) and the conductive polymer PEDOT:PSS. Preliminary experiments are done to determine substrate wettability and to characterize the electrical properties of the conductive ink. A substrate surface treatment is used to modify the wetting properties of the substrate. The effect of the surface treatment exposure time is evaluated by measuring the width of printed lines. The experiment results are used to evaluate the sensor structure printing process. IDE structure is fabricated by inkjet printing, and the piezoelectric layer is screen printed on top of the electrodes. Electrical properties and piezoelectric sensitivity of the final samples are characterized.

The results of this research show that the ink and substrate properties have an impact on the performance of the printed structures. The surface energy of the substrate is modified to improve its wettability. Thus, UV/O_3 surface treatment can be used to make Parylene-C hydrophilic. Furthermore, the IDE structure can be fabricated by inkjet printing technology. However, the coffeering effect is observed in narrow PEDOT:PSS inkjet printed lines (i.e. IDE fingers). This may have an impact on the conductivity of the lines due to the non-uniform distribution of the material. On the other hand, the validation of the piezoelectric sensitivity characterization suggests that the poling process has to be improved to guarantee the operation of the device as a piezoelectric sensor. The results of this research validate that ultra-thin sensors can be fabricated using printed electronics technologies. The overall thickness of the sensors is below 6 µm. In conclusion, further research has to be done to activate properly the piezoelectric properties of the P(VDF-TrFE) material in this sensor configuration.

Keywords: ultra-thin, IDE, P(VDF-TrFE), piezoelectric, flexible pressure sensor

PREFACE

This master's thesis work was done in the Laboratory for Future Electronics at the Electrical Engineering Unit, Faculty of Information Technology and Communication Sciences at Tampere University. This work is funded by Business Finland Project (Grant No. 2947/31/2018). This thesis work was supervised by Prof. Matti Mäntysalo and Dr. Mika-Matti Laurila.

I would like to thank Prof. Matti Mäntysalo for allowing me to work on this fascinating topic, and for his guidance and support. I would also like to thank Dr. Mika-Matti Laurila whose advice and comments were of great help, and for always having an answer to my questions concerning my research or writing. In addition, I would like to thank everyone at Laboratory for Future Electronics for having a pleasant working environment.

I would like to thank my mother and my sisters for their continued help and support, and for always being there for me. Last but not least, I would like to thank Jhonny for his unconditional love and support.

Tampere, 13 November 2019

Karem Lozano Montero

CONTENTS

LIST OF FIGURES

LIST OF SYMBOLS AND ABBREVIATIONS

2D	Two-dimensional
3D	Three-dimensional
CIJ	Continuous inkjet
CV	Coefficient of variation
DOD	Drop on demand
ECG	Electrocardiogram
E-skin	Electronic skin
FE	Finite element
IDE	Interdigitated electrodes
ILLO	Inorganic-based laser lift-off
MIM	Metal-insulator-metal
Parylene	Poly-para-xylylene
PDMS	Polydimethylsiloxane
PEDOT:PSS	Poly(3,4-ethylenedioxythiophene) polystyrene sulfonate
PET	Polyethylene terephthalateFE
PVDF	Polyvinylidene fluoride
P(VDF-TrFE)	Poly[(vinylidenefluoride-co-trifluoroethylene)]
PTFE	Polytetrafluoroethylene
PZT	Lead zirconate titanate
SWNT	Single-walled carbon nanotube
UV/O_3	Ultraviolet-ozone
ZnO	Zinc oxide

T	External stress
S	Strain
V	Voltage
E	Electric field
D	Surface charge density
e	Piezoelectric constant
h	Piezoelectric constant
d	Piezoelectric strain coefficient
g	Piezoelectric voltage coefficient
d_{31}	Transverse mode
d_{33}	Longitudinal mode
ε_r	Relative dielectric constant
ε_0	Dielectric constant of free space
A	Area
t	Film thickness
Q	Generated charge
σ_{xx}	Mechanical stress
g_{3j}	Piezoelectric voltage constant
ε^T	Material permittivity under a constant strain
R_T	Equivalent resistance
R_S	Sheet resistance
R	Line resistance
L	Line length
w	Line width
ρ	Resistivity

σ	Conductivity
STD	Standard deviation

1. INTRODUCTION

Vital signs are indicators that are monitored to check the human health status. The primary vital signs are body temperature, blood pressure, heart rate, electrocardiogram (ECG), and respiration rate [1]. Additionally, the continuous monitoring of these indicators could help to detect abnormalities and lead to the detection of diseases at an early stage. Traditionally, monitoring of vital signs has been done using rigid and bulky electronic devices. Thus, using these types of devices could be uncomfortable when monitoring is done continuously. Furthermore, the mechanical mismatch between the skin and the rigid devices could lead to measurement errors [2]. As a consequence, the development of skin-conformal devices needs to be studied. Skin-conformal devices are characterized by having a thickness below 10 μm [3]. Figure 1 illustrates some medical applications of skin conformal devices.

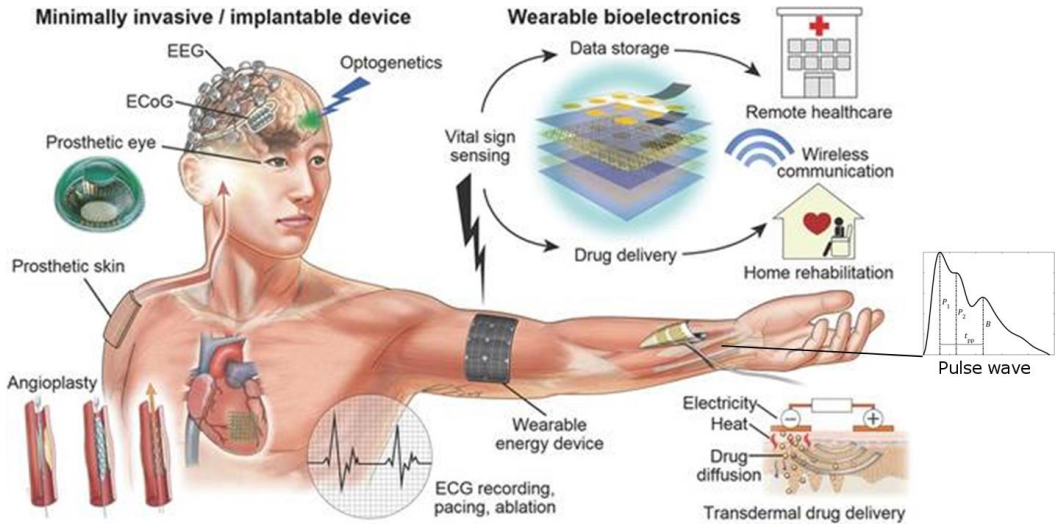

Figure 1. *Illustration of medical applications of skin-attachable devices. Adapted from [4].*

Lately, the research in the field of wearable monitoring systems is focusing on developing flexible and conformal devices which can be easily attached to the skin[5][6][7]. Self-powered ultra-thin flexible piezoelectric sensors for pulse monitoring have been reported [8]. However, the sensors utilize a lead-based piezoelectric material which has toxic effects. Furthermore, the fabrication limitations in scalability, associated with inorganic-based laser lift-off (ILLO) transfer process, reduces the cost-effectiveness. In contrast,

printed piezoelectric pressure sensors based on the piezoelectric polymer poly(vinylidenefluoride-co-trifluoroethylene) (P(VDF-TrFE)) have been demonstrated [9][10][11]. Using polymers and printed electronic technologies eliminate biocompatibility issues and decrease production costs. Nonetheless, the sensor is fabricated on a relatively thick substrate (>> 10 µm), and an adhesive patch must be used to attach the sensor to the skin.

Consequently, the development of ultrathin, low-cost, biocompatible sensors needs to be investigated. First, the ultra-thin feature makes the sensors skin-conformable [12][13]. Conformability decreases the mechanical mismatch between the skin and the sensor observed when thick and rigid sensors are placed on the skin. This feature should also facilitate the transmission of the signal across the skin-sensor interface. Furthermore, ultra-thin sensors can conform to the human skin which eliminates the need to use adhesives to attach the devices on the skin [2]. Second, using fabrication methods such as printed electronics technologies can considerably decrease the production costs and material waste in comparison to traditional processes such as transfer processes (e.g. ILLO) and photolithography [9][7][14]. Therefore, printed electronic technologies can be used to fabricate low-cost sensors. Additionally, the fabrication process is simplified by using these technologies [15]. Third, biocompatibility is a key property when sensors interface with biological tissues. Piezoelectric polymers, such as P(VDF-TrFE), are a promising class of materials to be used in medical applications because of being biocompatible and environment-friendly [11][16]. Moreover, these materials can be processed using printed electronics technologies which do not increase the fabrication costs. Furthermore, the sensor configuration could have an impact on the sensitivity of the sensor. Thus, sensors will be fabricated based on the interdigitated electrodes (IDE) structure. IDE configuration allows having access to a piezoelectric mode which leads to high piezoelectric sensitivity.

To summarize, the research aims to develop ultra-thin IDE piezoelectric pressure sensors using printing technologies. Sensors will be fabricated using inkjet printing and screen-printing technologies. The fabrication of the sensor will be done using biocompatible polymer materials. Furthermore, it is intended to use these sensors for pulse wave measurements. However, the application of these sensors is not limited only to healthcare. It is also possible to use them in robotics and prosthetics applications.

This thesis document is divided as follows. First, in Chapter 2 the piezoelectric sensors working principle and properties of different piezoelectric materials are explained. In addition, most common piezoelectric sensors configurations are also explored. Printing

technologies such as inkjet printing and screen-printing are also examined in this chapter. Chapter 3 describes all the experiments and fabrication processes used in this thesis for the fabrication of the ultra-thin IDE pressure sensors. Chapter 4 focuses on presenting and analyzing all the obtained results from this research. Finally, Chapter 5 summarizes the thesis outcomes, and future work is also presented in this chapter.

2. LITERATURE REVIEW

This section introduces the theoretical background of this thesis work. First, the piezoelectric sensors working principle is explained and the properties of some piezoelectric materials are given. In addition, most common structures used for implementing flexible and ultra-thin piezoelectric sensors are described. In addition, printing technologies are briefly described. Inkjet printing and screen-printing are explained in more detail because those technologies were used in this thesis.

2.1 Piezoelectricity

Piezoelectricity was discovered in 1880 by the Curie brothers; however, its use in practical applications was introduced after several years [17]. Piezoelectricity is an electromechanical phenomenon. This phenomenon occurs in response to an interaction between mechanical and electrical properties of a material such that mechanical deformation of the material causes a change in net polarization across the material. A material exhibits piezoelectricity if the structure of the material does not have a symmetry center. Owing to this characteristic, piezoelectric materials are a distinct type of dielectric materials that show transducer properties [18][19].

Piezoelectric materials are used in a wide variety of technical applications, for instance, in information and communications (e.g. battery-free systems), industrial automation(e.g. robotic systems), medical technology (e.g. vital signs monitoring devices), among others [17]. Recently, applications of piezoelectricity to wearable sensors and actuators have increased dramatically owing to the discovery of new low temperature and solution-processable materials (e.g. PVDF-family polymers), and new fabrication methods for devices (e.g. printing technologies). This is a vast research field, which can be divided into the study of synthesis and properties of piezoelectric materials, fabrication of devices, characterization techniques and potential applications [18].

2.1.1 Direct and indirect piezoelectric effect

Piezoelectric effect can be divided into direct and indirect piezoelectric effect [18]. The direct piezoelectric effect can be defined as the change of the net polarization when an external mechanical deformation is applied to the material. This deformation leads to electric displacement in the material. Thus, this can be detected as a change in the

amount of charges accumulated on the material surface. Figure 2 illustrates the direct piezoelectric effect. As seen in this figure, tensile or compressive stress can be applied to the material. As a result, a positive voltage is generated when tensile stress is applied parallel to the poling direction (Figure 2b). On the contrary, a negative voltage is generated when compressive stress is applied (Figure 2c). [19]

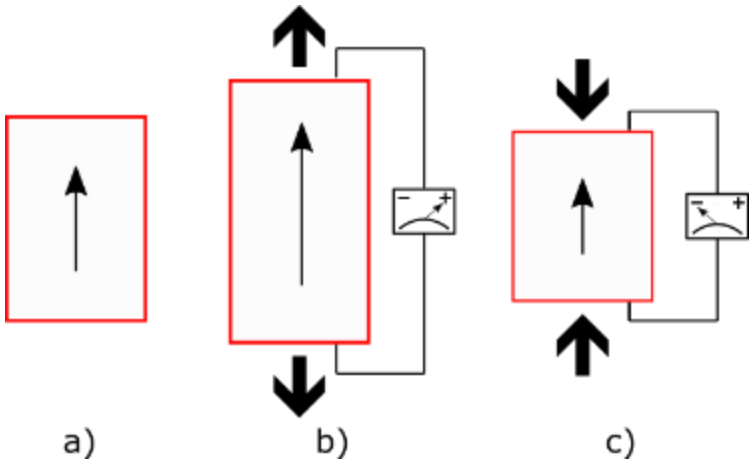

Figure 2. *Direct piezoelectric effect: a) tensile stress applied; b) compressive stress applied. Adapted from [19].*

On the other hand, the indirect piezoelectric effect results when applying an external electric field to the material. Figure 3 depicts the indirect piezoelectric effect. In this scenario, a mechanical strain is generated in response to the applied electric field. If the electric field is applied in the same direction as the polarity of the material, the material is stretched (Figure 3b). Otherwise, when the electric field is applied in the opposite direction, a compressive strain is generated in the material (Figure 3c) [19].

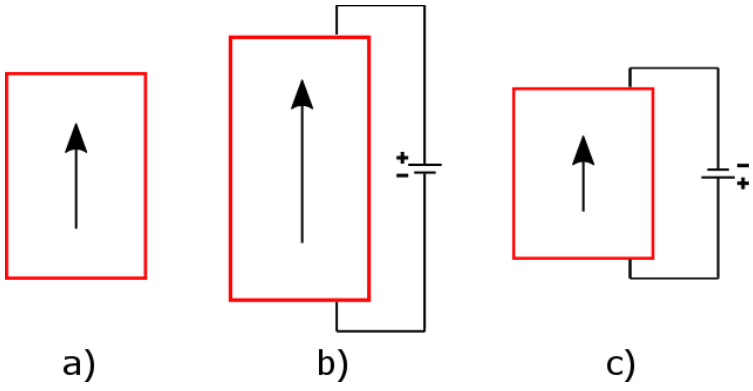

Figure 3. *Inverse piezoelectric effect: a) voltage with the same polarity; b) reverse voltage. Adapted from [19].*

Both effects have several applications owing to the conversion of electrical energy into mechanical energy and vice versa [18]. In Figure 4, it is shown a summary of some practical applications of piezoelectricity. The piezoelectric pressure sensor developed in

this thesis is based on the direct piezoelectric effect. Thus, a more detailed analysis of this effect is presented below.

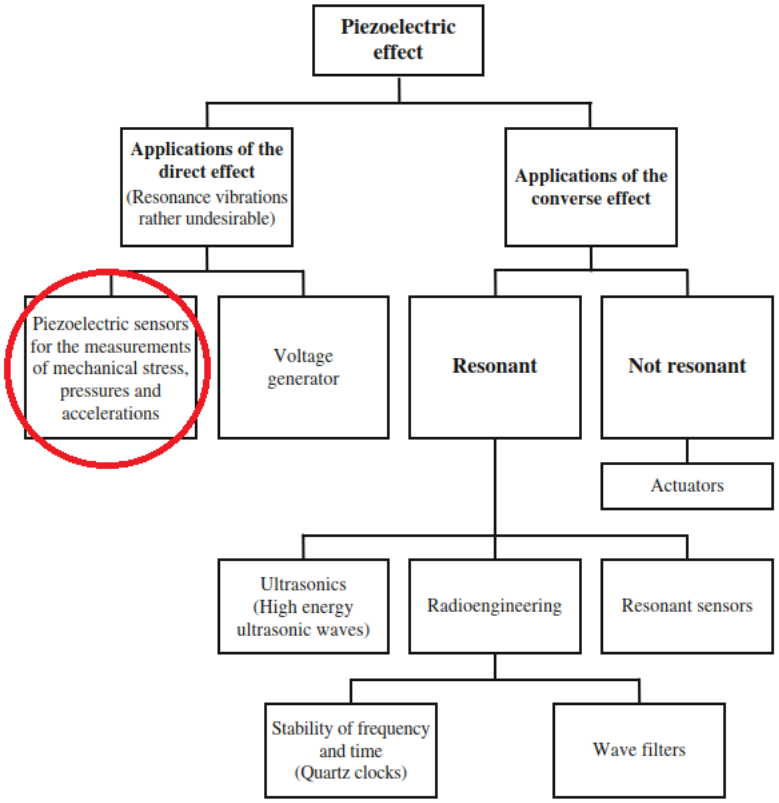

Figure 4. *Practical applications of piezoelectricity* [18].

The piezoelectric sensitivity of a piezoelectric material is described by the piezoelectric coefficients, which connect the input and output parameters (i.e. mechanical and electrical parameters). External stress (T) and strain (S) are forms to express the mechanical input. Electrical output can be in the form of electric field (E), or surface charge density (D) [19]. The equations that describe the relation between mechanical input and electrical output are detailed below.

$$D = dT \tag{1}$$

$$E = gT \tag{2}$$

$$D = eS \tag{3}$$

$$E = hS \tag{4}$$

Moreover, the piezoelectric coefficients (e, h, d, and g) define the direct piezoelectric effect. These coefficients can be described by the partial derivatives shown in Table 1.

Table 1. *Direct piezoelectric coefficients [19].*

Piezoelectric coefficient	Definition		Unit
d	$\frac{\text{polarization}}{\text{stress}}$	$d = \left(\frac{\partial D}{\partial T}\right)_E$	C/N
g	$\frac{\text{electric field}}{\text{stress}}$	$g = -\left(\frac{\partial E}{\partial T}\right)_D$	$V \cdot m/N$
e	$\frac{\text{polarization}}{\text{strain}}$	$e = \left(\frac{\partial D}{\partial S}\right)_E$	C/m^2
h	$\frac{\text{electric field}}{\text{strain}}$	$h = -\left(\frac{\partial E}{\partial S}\right)_D$	V/m

The coordinates system used to represent the direction of the poling and the stress is the right-handed Cartesian. Figure 5 illustrates this system. The X-, Y- and Z-axes are denoted by 1, 2, and 3, respectively. In addition, the rotations around the X-, Y-, and Z-axes are denoted by 4, 5, and 6. [19]

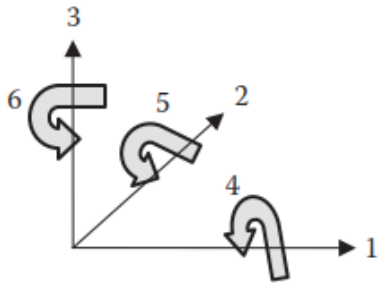

Figure 5. *Right-handed cartesian coordinate system* [19].

Equation (1) can be represented in terms of the T and D components. T is a tensor with components:

$$\begin{pmatrix} T_{11} & T_{12} & T_{13} \\ T_{21} & T_{22} & T_{23} \\ T_{31} & T_{32} & T_{33} \end{pmatrix}$$

T is also symmetric due to $T_{12} = T_{21}$, $T_{13} = T_{31}$, and $T_{32} = T_{32}$. Thus, it has only six independent components. In addition, D has the components:

$$\begin{pmatrix} D_1 \\ D_2 \\ D_3 \end{pmatrix}$$

Therefore, the electric displacement field can be also described by equation (5).

$$
\begin{aligned}
D_1 &= d_{111}T_{11} + d_{112}T_{12} + d_{113}T_{13} + d_{121}T_{21} + d_{122}T_{22} + d_{123}T_{23} + d_{131}T_{31} \\
&\quad + d_{132}T_{32} + d_{133}T_{33} \\
D_2 &= d_{211}T_{11} + d_{212}T_{12} + d_{213}T_{13} + d_{221}T_{21} + d_{222}T_{22} + d_{223}T_{23} + d_{231}T_{31} \\
&\quad + d_{232}T_{32} + d_{233}T_{33} \\
D_3 &= d_{311}T_{11} + d_{312}T_{12} + d_{313}T_{13} + d_{321}T_{21} + d_{322}T_{21} + d_{322}T_{22} + d_{323}T_{23} \\
&\quad + d_{331}T_{31} + d_{332}T_{32} + d_{333}T_{33}
\end{aligned} \tag{5}
$$

These equations can be simplified as denoted in equations (6). In these equations, the indexes 1, 2, and 3 represent tensile or compressive stress (or strain) and 4, 5, and 6 denotes shear stress (or shear strain). [19].

$$
\begin{aligned}
D_1 &= d_{11}T_1 + d_{12}T_2 + d_{13}T_3 + d_{14}T_4 + d_{15}T_5 + d_{16}T_6 \\
D_2 &= d_{21}T_1 + d_{22}T_2 + d_{23}T_3 + d_{24}T_4 + d_{25}T_5 + d_{26}T_6 \\
D_3 &= d_{31}T_1 + d_{32}T_2 + d_{33}T_3 + d_{34}T_4 + d_{35}T_5 + d_{36}T_6
\end{aligned} \tag{6}
$$

Many of the materials employed in sensor and actuator applications are isotropic. These materials lose the isotropic property after the poling process. The poling direction usually is in the Z-direction. Then, owing to the system properties after poling, the system is cylindrically symmetric. As a result, the number of independent piezoelectric components decreases. Then, the piezoelectric coefficient matrix is defined by equation (7). It is assumed that $d_{13} = d_{31}$ and $d_{15} = d_{51}$. Therefore, the piezoelectric properties of a poled material are defined by the coefficients d_{31}, d_{33}, and d_{15}. These piezoelectric coefficients express the relation between the charge collected on the electrodes and the applied mechanical stress. [19]

$$
d = \begin{pmatrix} 0 & 0 & 0 & 0 & d_{15} & 0 \\ 0 & 0 & 0 & d_{15} & 0 & 0 \\ d_{31} & d_{31} & d_{33} & 0 & 0 & 0 \end{pmatrix} \tag{7}
$$

The d_{31} coefficient is named the transverse mode. Equation (8) defines the direct piezoelectric effect when the external stress is in direction 1 on face 1 (X-axis) and the charge response is on face 3 (Z-axis). The d_{33} coefficient defines the direct piezoelectric effect when the external stress is in direction 3 on face 3 (Z-axis); the charge response is also on face 3 (Z-axis). This is called the longitudinal mode. Equation (9) represents the relation between D, T, and d_{33}. Furthermore, the coefficient d_{15} is called the shear mode. Equation (10) defines the direct piezoelectric effect when the stress is applied parallel to face 1 (direction 3), and the response is the charge on face 1. [19]

$$
D_3 = d_{31}T_1 \tag{8}
$$

$$D_3 = d_{33} T_3 \quad (9)$$

$$D_1 = d_{15} T_5 \quad (10)$$

2.1.2 Poling process

To induce piezoelectricity in piezoelectric materials, it is necessary to pole the material. The poling process is performed by applying a high electric field to the material to generate net remanent polarization [19]. Figure 6 illustrates the poling process. Dipoles are randomly oriented before the poling as can be seen in Figure 6a. When the electric field is applied to the material, the electric dipoles get oriented in the direction of the applied field (Figure 6b). Then, if the electric field exceeds the coercive field of the material, most of the dipoles are oriented in the same direction after the poling process (Figure 6c). This results in maximum material polarization. This process requires a set of steps. For certain materials, it is first necessary to heat the material to a temperature below the Curie temperature or stretch it. Next, a high electric field is applied to the material [20]. The most common methods used for performing this process are corona poling and direct poling [21].

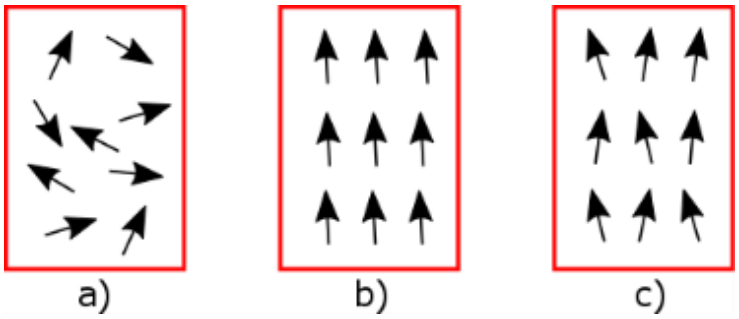

Figure 6. *Poling process: a) non-poled material; b) during poling; c) after poling. Adapted from [19].*

The corona poling method is performed by applying an electric field to the material through a needle that is kept under a certain distance from the material. This method is depicted in Figure 7a. As can be seen in the figure, the material is placed on a base plate, and voltage is applied to the needle and the base. In addition, the base plate temperature is increased until it reaches the material glass transition temperature. Once the needle reaches the ionizing energy of the adjacent air, ionic species are created and attracted to the plate. After enough surface charge density is created, the ions flow towards the base plate through the thickness of the material [22]. This process results in the polarization of the material. On the contrary, the direct poling method is done by

applying the electric field directly to the electrodes that are in contact with the piezoelectric material. The direct poling method is illustrated in Figure 7b. As depicted in this figure, the piezoelectric material is distributed between two parallel electrodes. Thus, the poling electric field is applied to the electrodes.

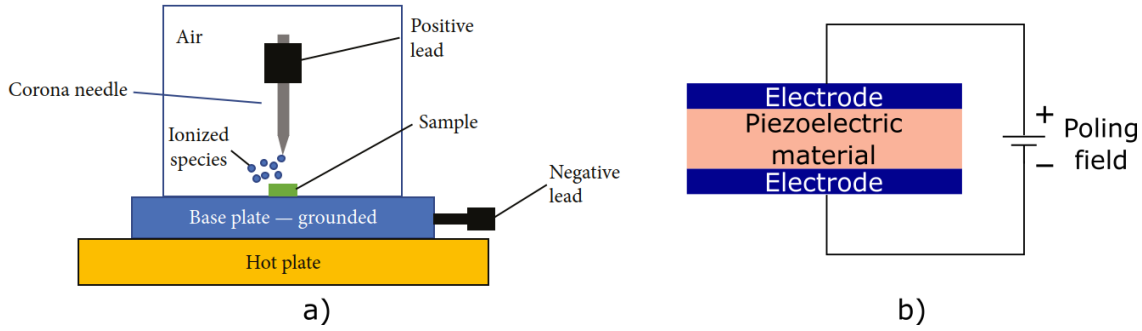

Figure 7. *Poling methods: a) corona poling method* [22]*; b) direct poling method.*

However, the materials should work under certain conditions to maintain the piezoelectric properties after polarization. According to [23], three main conditions should be fulfilled to maintain the piezoelectric properties. First, the temperature of the material should be maintained below its Curie temperature. Second, the material should not be under very strong alternating electric fields or direct fields, opposite to the polarization direction. Third, the mechanical stress applied to the material should not surpass a specific limit. Failing in fulfilling these requirements, the piezoelectric properties could be weaker or could be vanished.

2.1.3 Piezoelectric materials

Piezoelectric materials belong to a material group that is characterized by their noncentrosymmetric crystal structure. Depending on their structural features, these materials can be classified into four groups: ceramics, single crystals, polymers, and composites. Ceramics are polycrystalline materials that are formed by several crystal “grains” that have identical chemical composition. However, the ions in the grains can be orientated differently from one grain to other and the distance between ions can be slightly different. In contrast, single crystals have their positive and negative ions distributed periodically. On the contrary, polymers are materials composed of hydrogen and carbon atoms. These materials are based on long polymer chains that are composed of repeated units called “monomers”. The main advantage of these materials is that they are more flexible than ceramics and single crystals. In addition, composites are formed when some materials from the previous groups are combined to get certain properties. [24]

Previously, inorganic materials such as lead zirconate titanate (PZT) and zinc oxide (ZnO) nanowires were broadly studied owing to their high piezoelectric sensitivity. However, these types of materials present some disadvantages such as expensive production costs, stiffness, and biocompatibility issues due to lead content. On the other hand, there is a tendency for developing devices based on organic piezoelectric materials such as polymers. These materials are being highly investigated because of their high mechanical stability and compatibility with low-cost processing technologies [25]. The properties of piezoelectric materials play a major role in the device application. For flexible pressure sensors used in medical applications, it is desired to use materials with properties such as low-cost production, high mechanical stability, high piezoelectric coefficient, simple processing, and biocompatibility [26][27]. Table 2 summarizes the main properties of some piezoelectric materials.

Recently, most of the research done in this field make effort to develop flexible pressure sensors using piezoelectric materials that are biocompatible and can be implanted or attached directly to the human skin [28][29]. Therefore, polymer piezoelectric materials are excellent candidates to be used in this type of application. Polymeric piezoelectric materials are characterized for being flexible, mechanically stable, and can be processed as large-area thin films. Furthermore, these materials can be processed at lower temperatures compared to inorganic materials. In addition, these materials are compatible to be processed using solution processing methods such as spray coating, spin coating, doctor blade coating, screen printing, and inkjet printing, among others [27]. Although polymer piezoelectric materials have lower piezoelectric coefficients than ceramic materials, their compatibility with the aforementioned cost-effective fabrication technologies has enabled their wide use in sensor applications [3]. All the advantages associated with organic and polymeric materials allow developing flexible pressure sensors with outstanding properties.

Table 2. *Piezoelectric materials properties.*

Material	Type	Piezoelectric Constant d_{33} (pC/N)	Remanent Polarization ($\mu C/cm^2$)	Temperature (°C)	Coercive Field (V/µm)	Solution Processa-bility	Bio-compat-ibility	References
PbTiO3	Ceramic	117 to 143	8	600 to 900	40	Yes	Toxic	[38][39]
BaTiO3	Ceramic	149	> 50	850	7 to 16	Yes	Toxic	[36][37]
PZT	Ceramic	289 to 380	33	600 to 750	4	Yes	Toxic	[32][35]
ZnO	Ceramic	12	-	500 to 700	-	Yes	Low toxicity	[32][33][34]
PVDF	Polymer	-35	6.2	135 to 145	50	Yes	Non-toxic	[31][32]
PVDF-TrFe	Polymer	-24 to -30	7	135 to 145	45	Yes	Non-toxic	[30]

2.1.4 PVDF and its copolymer P(VDF-TrFE)

The most used and studied piezoelectric polymer is polyvinylidene fluoride (PVDF) and its copolymer with trifluoroethylene (P(VDF-TrFE)) [29][40]. PVDF material has a semi-crystalline structure with crystalline and amorphous regions, and its crystallinity is between 40% and 60%. The piezoelectric inactive amorphous regions decrease the effective piezoelectric performance of the material when compared to single or polycrystalline ceramic materials [18]. For instance, P(VDF-TrFE) has a charge piezoelectric coefficient d_{33} of -24 to -30 pC/N while ceramic materials such as PZT and BaTiO3 have a higher charge piezoelectric coefficient as can be seen in Table 2.

In addition, PVDF exhibits at least four different crystal phases α, β, γ, and δ depending on the fabrication conditions. The phase that exhibits strong piezoelectricity is the β-phase. Nevertheless, after the material crystallization, the non-polar α-phase is mostly observed. β-phase can be obtained by stretching the material when it is in the α-phase or by applying a high electric field to the material when is in α-phase and δ-phase [40]. In addition, the poling process is recommended to be done under thermal treatment [18]. Figure 8 illustrates the distribution of the crystal grains of PVDF before and after the poling process. Figure 8a illustrates the morphology of PVDF which is characterized by having crystalline regions scattered within amorphous regions. Figure 8b represents the stretching of the material. This process is done to align the crystalline regions and facilitate the rotation of the dipoles during the poling process. The orientation of the crystalline regions after poling is represented in Figure 8c.

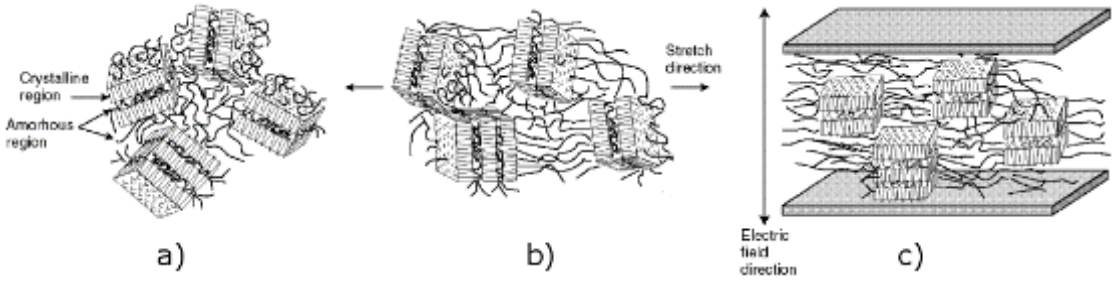

Figure 8. *PVDF schematic crystal structure: a) melt cast; b) mechanically oriented; c) electrically poled. Adapted from* [41].

In contrast, the copolymer formed with TrFe can reach a crystallinity of up to 90% [40]. P(VDF-TrFE) copolymer can be transformed directly to β-phase when the proportion of TrFe is higher than 20 % without applying a specific post-treatment [42]. The piezoelectric properties of P(VDF-TrFE) are owing to the remanent polarization obtained by aligning the internal dipoles of the crystalline phase by applying a strong electric field [43].

Thus, this material requires less fabrication steps during the fabrication process compared to PVDF fabrication, where stretching and thermal treatment are required. In addition, P(VDF-TrFE) is characterized by its high flexibility, great chemical resistance, and biocompatibility. These features make it an excellent candidate for flexible pressure sensors used for health monitoring. Moreover, P(VDF-TrFE) can be processed using printing technologies methods because it is soluble in common polar solvents (e.g. water, ethanol, methanol), and can be adjusted to the different solution-based fabrication methods [9].

2.2 Flexible and ultra-thin piezoelectric pressure sensors

Recently, flexible piezoelectric pressure sensors have drawn wide interest in the research community. For example, the PVDF based piezoelectric sensors offer advantages such as higher flexibility, low-cost fabrication, biocompatibility, and compatibility with large-area fabrication processes. There is a broad range of applications where these sensors can be used such as flexible electronic skin (E-skin) (e.g. soft robotics, prosthetics), healthcare monitoring (e.g. pulse-wave measurements), wearable devices (e.g. smart wristband), and industrial applications (e.g. structural health monitoring) [27][26].

Additionally, ultra-thin piezoelectric sensors are a sub-category of flexible piezoelectric sensors which are characterized by having a total thickness under 10 µm [44][45][13]. These type of sensors are being highly developed for biomedical applications. The trend in this research field is to fabricate sensors that can be attached directly to the human skin. Therefore, the ultra-thin characteristic makes the sensors skin-conformable which eliminates the drawbacks of thick and rigid sensors. This feature improves the quality of the acquired signals from the skin. Furthermore, ultra-thin piezoelectric sensors are more sensitive to mechanical deformations [2]. Nevertheless, their reusability is limited because of their softness and minimal thickness. Thus, using fabrication methods, such as printing technologies, minimizes fabrication costs and material consumption [12].

In particular, polymer piezoelectric materials are widely used in this type of sensors because they can be used for detecting deformations produced by small forces, mechanical vibration, bending, elongation or compression. Moreover, the fabrication of flexible piezoelectric sensors based on polymers is mostly based on thin-film geometries [46]. A thin-film can be described as a layer of material with a thickness fluctuating between several nanometers to some micrometers. Among piezoelectric polymers, P(VDF-TrFE) is an optimal piezoelectric material because of its chemical inertia, flexibility, simple fabrication, and large piezoelectric coefficient [47].

Further, the most common modes used for piezoelectric applications are d_{31} and d_{33}. The main difference between d_{31} and d_{33} modes is the direction of the generated electric field. In mode d_{31}, the electric field is perpendicular to the direction of the applied mechanical stress. On the other hand, the electric field is parallel to the direction of the applied mechanical stress in mode d_{33}. However, during bending stress, various piezoelectric coefficients are activated and their relative strength will determine the overall response of the sensors to the applied bending force. The most common structures used in flexible and ultrathin piezoelectric sensors are the metal-piezoelectric(dielectric)-metal (MIM) and interdigitated electrodes (IDE) structures [48].

2.2.1 MIM-based sensors

In MIM-based sensors, the piezoelectric material is distributed between two conductive electrodes. The sensing layer is deposited onto the bottom electrode before the top electrode deposition. Figure 9 illustrates the front and cross-sectional view of a MIM-based device, and the relative direction of the electric field between the electrodes. Some challenges could arise when fabricating this type of sensors using printing technologies. For example, non-uniform layers can increase the risk of short-circuit between the electrodes, and dielectric breakdown could happen during the film poling process. The poling electric field is determined by the piezoelectric material thickness [49].

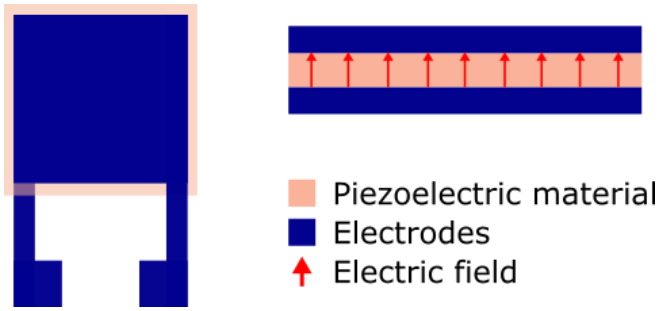

Figure 9. *MIM-based device.*

MIM structure is directly related to the parallel plate capacitor structure. The capacitance of a MIM-based sensor is mainly determined by the piezoelectric material thickness. Therefore, the capacitance of a sensor based on the parallel plate configuration can be calculated based on the material properties and structure dimensions (i.e. piezoelectric layer thickness) using the equation (11). Where A represents the overlapping area between the electrodes, ε_r is the relative dielectric constant of the piezoelectric material, ε_0 is the dielectric constant of free space, and t the thickness of the piezoelectric film.

$$C = \frac{\varepsilon_r \varepsilon_0 A}{t} \tag{11}$$

Moreover, the output voltage can be calculated if the generated charge Q and the capacitance values are known using equation (12).

$$V = \frac{Q}{C} \tag{12}$$

Furthermore, the voltage can also be expressed in terms of the piezoelectric constants. In general, when force is perpendicular to the electrode surface, charge generation is based on d_{33}, and when the force is parallel to electrode surface d_{31} is activated. Equation (13) describes the voltage in terms of mechanical stress (σ_{xx}), piezoelectric voltage constant (g_{3j}), and the thickness of the piezoelectric material (t).

$$V_{3j} = \sigma_{xx} g_{3j} t \tag{13}$$

In addition, g_{3j} can be defined as equation (14). d_{3j} represents the charge piezoelectric coefficient, and ε^T represents the material permittivity under a constant strain.

$$g_{3j} = \frac{d_{3j}}{\varepsilon^T} \tag{14}$$

Therefore, the output voltage can also be calculated using the piezoelectric charge constant (d_{3j}) and the material permittivity using equation (15).

$$V = \sigma_{xx} \frac{d_{3j}}{\varepsilon^T} t \tag{15}$$

2.2.2 IDE-based sensor

In IDE-based sensors, the term “interdigitated” is referred to a finger-like pattern repeated periodically. The main difference between IDE and MIM structures is the distribution of the materials. In IDE configuration, a thin layer of conductive material is distributed on the substrate to build two electrodes with an interdigitated approach, and the active material is deposited on top of the electrodes. Figure 10 illustrates the front and cross-sectional view of an IDE-based sensor. The working principle of IDE structures is similar to the MIM structure, but in this case, the piezoelectric effect occurs between each pair of successive electrodes. Thus, IDE geometry is based on a set of cells. A pair of contiguous electrode fingers composes each cell. Piezoelectric effect occurs in each cell owing to the piezoelectric material between the fingers [48]. In addition, using the IDE structure requires less processing steps during the sensor fabrication process. This geometry also decreases the possibility of short-circuit between the electrodes in comparison to the

MIM structure. In this configuration, the poling field is determined by the distance between IDE fingers [49].

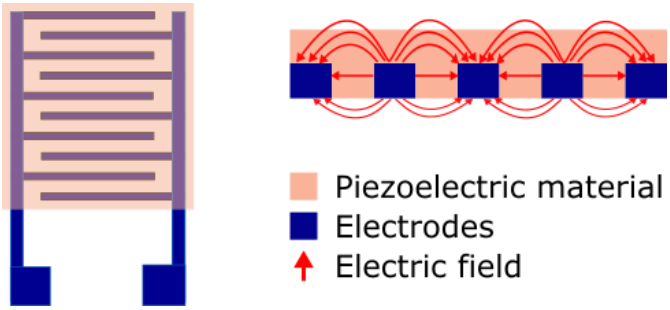

Figure 10. *IDE-based device.*

Although the IDE structure working principle can be explained based on the MIM structure approach (i.e. equation (12)), the underlying equations that describe different parameters such as capacitance, electric field or generated charge are not the same in both cases. More complex equations are needed to calculate IDE-based sensors characteristic parameters [50][51]. Nevertheless, the output voltage can be also calculated using the piezoelectric coefficients as in MIM-based sensors, using equation (16).

$$V_{33} = \sigma_{xx} g_{33} t = \sigma_{xx} \frac{d_{33}}{\varepsilon^T} t \tag{16}$$

2.2.3 MIM and IDE comparison

A comparison of a MIM and IDE sensor can be done based on the illustration in Figure 11. When the applied stress is parallel to the electrodes, the MIM sensor works in d_{31} mode (Figure 11a). On the other hand, an IDE sensor works in d_{33} mode under the same conditions (Figure 11b). Therefore, an IDE sensor can generate a higher output voltage compared to a MIM sensor with the same piezoelectric material thickness and area. This is because the magnitude of the piezoelectric coefficients d_{33} and g_{33} are higher than d_{31} and g_{31} [49]. Furthermore, MIM-based sensors are characterized by having a higher capacitance than IDE-based sensors [52]. Thus, a higher capacitance value leads to a low output voltage as described in equation (12). On the contrary, a higher output voltage is obtained when the capacitance is low.

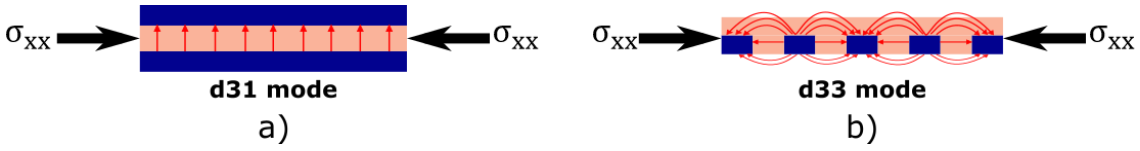

Figure 11. *Schematic of a) MIM-based sensor on d_{31} mode and b) IDE-based sensor on d_{33} mode.*

Table 3 lists the main characteristics of previously reported studies about thin flexible piezoelectric pressure sensors. Reported studies about IDE-based pressure sensors are lower compared to MIM-based sensors. This is because of the difficulty of IDE structure fabrication. However, using the IDE structure reduces the number of processing steps which eliminates possible challenges related to annealing conditions when printing multiple layers as in MIM-based sensors fabrication. Therefore, owing to the characteristics of IDE-based sensors (i.e. higher output voltage and less fabrication steps), developing piezoelectric pressure sensors based on this configuration can be advantageous.

Table 3. *Summary of reported flexible piezoelectric pressure sensors.*

Material	Structure	Sensitivity	Thick-ness	Fabrica-tion method	Refer-ence
PZT	IDE	0.018 kPa^{-1}	< 10 µm	ILLO	[8]
P(VDF-TrFE)	MIM	0.8 $V{\cdot}MPa^{-1}$	> 50 µm	Screen printing	[9]
P(VDF-TrFE)/MWCNT	MIM	0.04 V/N	> 50 µm	Screen printing	[14]
P(VDF-TrFE)	MIM	-	> 50 µm	Inkjet printing	[10]
P(VDF-TrFE)	MIM	0.008 – 0.185 $V{\cdot}kPa^{-1}$	> 50 µm	Electrospin-ning	[11]

2.3 Printing Technologies

Printed electronics is a category of electronic devices, which are fabricated employing printing technologies. Usually, these printing technologies have their origins in the graphic industry and are referred to the traditional printing methods [5]. The main printing technologies used for fabricating electronics are flexography, gravure, offset, screen, and inkjet printing. The main difference between the traditional printing methods and printed electronics technologies is that in the latter case electrically functional inks are employed. Electrically functional inks have conducting, semiconducting, and dielectric properties [5]. For instance, some functional inks are nanoparticle silver inks, single-

walled carbon nanotube (SWNT) based inks, and polydimethylsiloxane (PDMS). Furthermore, piezoelectric inks (e.g. PVDF, and P(VDF-TrFE)) are a subcategory of dielectric inks that can be processed using different printing technologies, such as screen printing and inkjet printing. In addition, the ability to process these materials at low-temperatures has made them compatible with ultra-thin and flexible substrates that employ low glass transition temperature polymers. This feature has increased the interest of developing ultra-thin flexible electronic devices owing to the wide range of applications where these devices can be used (e.g. E-skin applications, healthcare monitoring devices).

Secondly, printing technologies have many advantages compared to traditional fabrication processes. The main benefit is the reduction of tooling and material costs during the process. Printing is an additive method, as a result, only the required materials are utilized. Thus, there is less material waste compared with traditional subtractive methods used for fabricating electronics. Generally, the fabrication of electronic devices using traditional methods is characterized by the use of complex and expensive processes such as photolithography [53].

On the other hand, the selection of the printing technology is not straightforward. Several parameters determine the most suitable technology for the desired application. In addition, there is not a single choice for one application. The selection of the printing technology is usually made based on the required resolution, functional ink, and substrate. The printing technologies chosen to develop this research work were inkjet printing and screen-printing. Further details of the working principles of these technologies are explained in the next sections.

2.3.1 Inkjet Printing

Inkjet printing is characterized by being a non-contact printing technology. This technology is mostly based on two methods for drop generation: continuous inkjet (CIJ) and drop-on-demand (DOD). When this technology is based on the CIJ method, the flow of the fluid going through the nozzles is continuous. While in the case of the DOD method, drops are formed only when they are required. Comparing both methods, CIJ based systems are more complex than DOD based because the CIJ systems must have a method to generate drops, a method to choose the drops, and a method to retrieve and dispose the liquid [54]. In this thesis, only DOD based inkjet printing is presented, as this is the method selected to fabricate the sensors developed in this work.

DOD printing systems are classified based on the type of actuator that is used for the droplet ejection mechanism. The most common methods are based on piezoelectric or

thermal components. In thermal DOD (Figure 12a), there is a small heating element in contact with the ink reservoir. When this element is heated, the ink starts to evaporate and a vapor bubble is created. The expansion of the vapor bubble generates the fluid displacement and energy needed to drive a droplet through the nozzle [54].

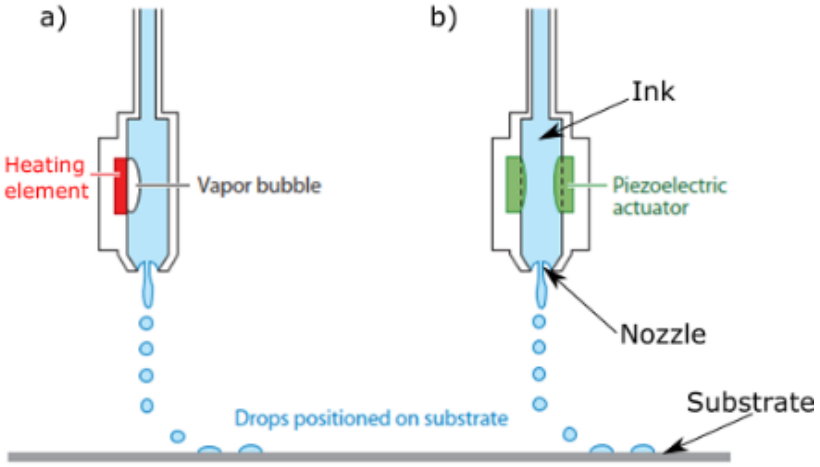

Figure 12. *Schematic of thermal and piezo DOD principles: a) thermal DOD; b) piezo DOD. Adapted from* [55].

On the other hand, when a piezoelectric actuator is used, the drop ejection is generated when the piezoelectric actuator is deformed. The deformation of the piezoelectric actuator changes the internal pressure of the ink reservoir which produces pressure waves in the ink chamber. Thus, this process results in the ejection of the ink through the nozzles. The parameters that define the initial droplet ejection are the piezo drive waveform, frequency, and voltage amplitude. All these parameters can be configured using the printer software. The deformation of the piezoelectric component is mainly controlled by applying a specific voltage waveform to it. In Figure 13, it can be seen drops ejected from an inkjet printer. It should be noted that the waveform design depends on the fluid. Thus, it is not possible to use the same waveform to print different types of inks. [56]

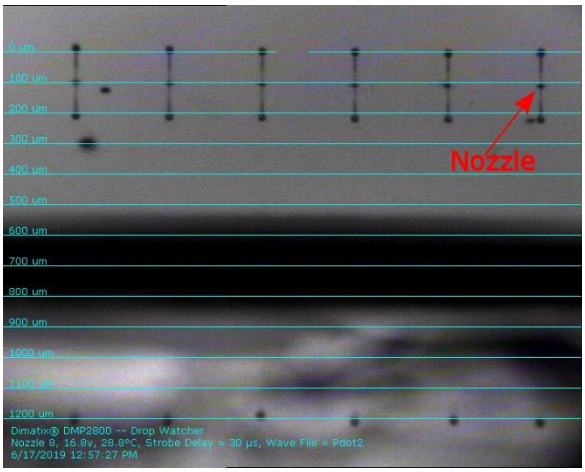

Figure 13. *Firing nozzles.*

This technology presents some advantages. For example, it avoids damaging of previously printed layers, as it is a non-contact technology. An important advantage of this technology is its compatibility with fluids with low viscosity. Thus, inks that are not compatible with other technologies can be deposited using inkjet printing [56]. Additionally, using this technology is possible to customize the pattern to be printed. Patterns can be designed using the printer software or an image editor software.

On the other hand, some issues can arise when using inkjet printing technology. If the manufacturer does not supply the waveform, its design process can be time-consuming. In addition, another possible limitation at lab-scale is the limited number of nozzles. This can make the printing process very slow. Further, the jetting process is very sensitive to changes in the rheological properties of the ink, which can lead to the clogging of the nozzles. Clogging may also happen if the particle size of the ink becomes too large due to the agglomeration of the particles. In certain cases, this issue can be solved by cleaning the nozzles, but sometimes the cartridge needs to be replaced. Moreover, as the ink jetting is not continuous, possible changes in the ink, such as solvent evaporation from the ink meniscus at the nozzle, can have a negative impact on the nozzle performance [54][56].

2.3.2 Screen Printing

Screen-printing is an old technology, which has been adapted for the fabrication of electronic devices in the last decades. The screen-printing process is depicted in Figure 14. As can be seen in this figure, a screen is placed above the substrate. The screen is composed of a mesh attached to a metallic frame. Further, the gap between the screen and the substrate has an impact on printing quality. The screen mesh contains the de-

signed pattern of homogenous thickness. The ink is poured on the screen using a flooding plate or a metal squeegee without applying any pressure to the screen mesh (Figure 14a). Then, a local stress is applied to the screen mesh using a polymeric or metal squeegee (Figure 14b). Thus, the ink is pressed through and put in contact with the substrate. The printing process is done at low printing pressure. [56]

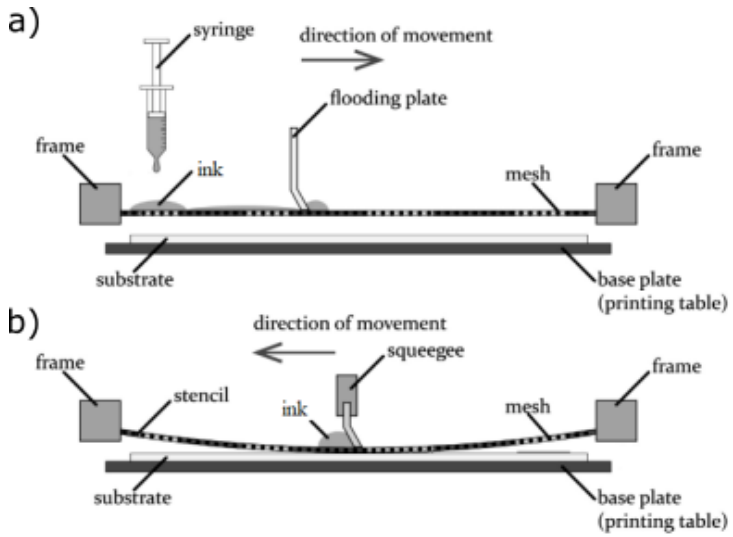

Figure 14. *Screen printing process: a) ink poured onto the screen; b) ink pressed through the screen. Adapted from [56].*

In addition, several parameters have an impact on the printing quality. For instance, mesh type, ink viscosity, print speed, and squeegee angle. Patterns printed using screen-printing technology do not exhibit the same printing quality that can be obtained with printing technologies such as inkjet, gravure or flexography. In comparison with other technologies, using screen printing is possible to print high aspect ratio objects. The thickness of materials printed using this technology are in the order of tens of microns. Further, it is possible to print thicker patterns with thicknesses higher than 100 µm with a single pass; this cannot be produced using any other printing technology [57]. The main printing defect observed, when using this method, is the inaccuracy of the edges of the printed patterns. Furthermore, the roughness of the printed layers is higher compared with other techniques. Resulting from the adhesion of the printed fluid to the mesh fibers during the printing process [56].

3. MATERIALS AND METHODS

This section describes the materials and equipment used in this work. Moreover, the experiments executed to analyze the properties of the materials are explained. The results obtained in these tests were used in the sensor design process. Furthermore, the fabrication process of the final samples is reported. Finally, electrical characterization setup and sensitivity measurement setups are explained.

3.1 Materials

The fabrication process steps are illustrated in Figure 15. The fabrication process starts with the deposition of a release layer onto the carrier (Figure 15a). Then, the substrate material is deposited (Figure 15b). Next, the electrodes are fabricated using inkjet printing (Figure 15c) and the piezoelectric material is deposited by screen printing (Figure 15d). Further, a second layer of Parylene-C is deposited as a protection layer (Figure 15e). Finally, the sensors are peeled off from the carrier (Figure 15e). All the materials and the equipment used in each fabrication step are described in this section.

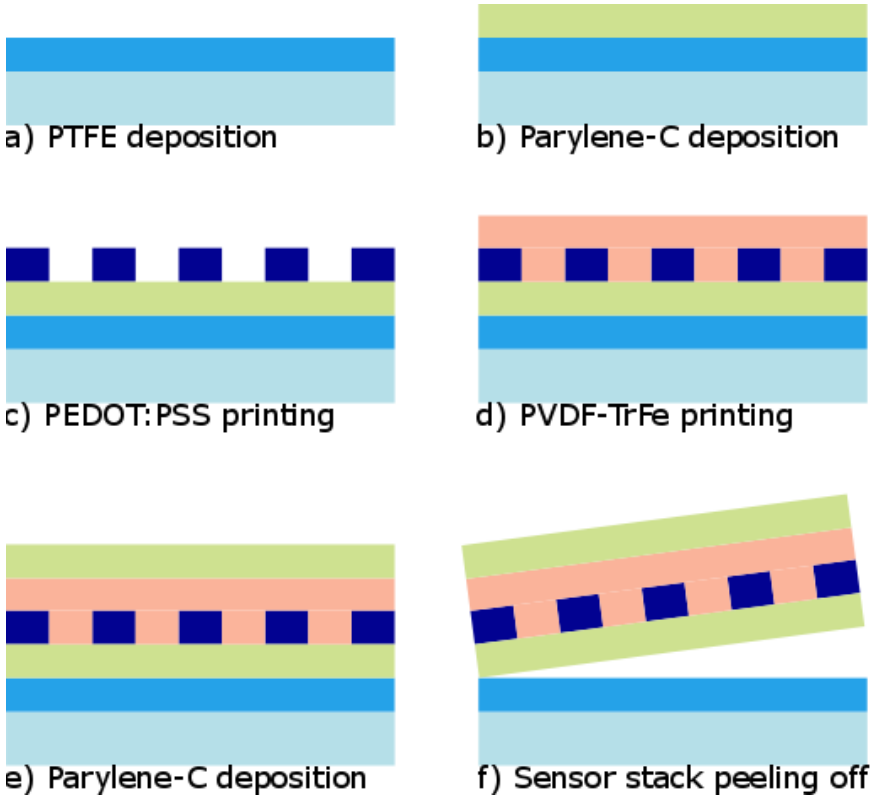

Figure 15. *Schematic of the sensor fabrication process, cross-section view. The fabrication process is described above.*

3.1.1 Substrate

The thesis aimed to fabricate an ultra-thin flexible sensor that is highly skin-conformable and can be placed on the human skin without the use of adhesives. For this reason, the sensor had to be fabricated in a substrate with excellent mechanical properties such as high flexibility. In addition, the material should be biocompatible. To meet the required specifications, poly-para-xylylene (Parylene) was chosen as a substrate. Parylene is a class of polymer, which is semi-crystalline and hydrophobic. This polymer can be deposited as thin, conformal, and pinhole-free films using chemical vapor deposition. There are many types of parylene, for instance, Parylene-N, Parylene-C, Parylene-D, and Parylene-HT. [58]

In this work, the material used was Parylene-C. This material has been widely used in biomedical applications owing to its biocompatibility, and chemical and solvent inertness. Furthermore, this material can be deposited without using any extra harmful chemicals [59]. During the fabrication process, Parylene-C can also be deposited onto a temporary substrate. When all the fabrication processes are completed, it is easy to peel off the whole materials stack from the carrier, if the carrier has been coated with a release layer. Parylene-C is a transparent, highly flexible, and durable material. Further, thicknesses of Parylene layers can be in the order of few microns, and even 150 nm thick layers have been demonstrated for transistor gate dielectrics [12][60]. These features make it an excellent candidate to be used as a substrate in ultra-thin and flexible electronics applications.

The compound GALXYL C from Galentis S.r.l. manufacturer was used as a substrate in this work. The temporary carriers, where this material was deposited, were glass wafers with a thickness of approximately 1200 µm. Before doing the Parylene-C coating, glass substrates were cleaned to eliminate surface contamination. Next, polytetrafluoroethylene (PTFE) was deposited by a spin-coating process. This step was required to facilitate the Parylene-C layer peel off. Then, Parylene-C was deposited on the carriers using the LabTop 3000 ParaTech coating machine depicted in Figure 16.

Figure 16. *Parylene coating machine*

3.1.2 Inks

For this research, it was used two types of commercial inks. The conductive material used to print the electrodes was the conductive polymer poly(3,4-ethylenedioxythiophene):poly(styrene sulfonate) (PEDOT:PSS). The ink Clevios P Jet CEO 3 was purchased from Heraeus manufacturer. The ink properties are detailed in Table 4.

PEDOT:PSS is an electrolyte composed of two polymers. PEDOT is positively charged, and PSS is negatively charged. The function of PSS is also to promote the dispersion and stabilization of PEDOT in the used solvent. The conductive polymer PEDOT:PSS is highly used in practical applications such as sensors, energy harvesters, and photovoltaic cells. The advantage of using this material is that it is possible to form a homogenous thin film on rigid or flexible substrates. This polymer can be processed using different methods such as spin casting, doctor blade, inkjet printing or screen-printing. Furthermore, PEDOT:PSS printed films exhibit good conductivity when compared to other conductive polymers. Flexibility is also a key property of this material. All these properties make it an excellent candidate to be used in flexible printed electronics. [61]

On the other hand, the piezoelectrically active layer was printed using a piezoelectric ink. The piezoelectric ink used in this work was the commercial ink Piezotech FC 20 from Arkema. This ink is a P(VDF-TrFE) printable electroactive polymer formulation. The main

properties of this ink are summarized in Table 4. The ink does not need any pre-conditioning before printing and can be stored at room temperature. To activate the piezoelectric properties of the material, a poling process is required. According to the manufacturer specifications, for thin printed layers, the poling electric field can be applied directly to the electrodes that are in contact with the piezoelectric layer. The poling setup used in this work is detailed in section 3.1.5.

Table 4. *P(VDF-TrFE) and PEDOT:PSS ink properties [30][62].*

Piezotech FC 20 P(VDF-TrFE)	
Annealing T (ºC)	135
Annealing time (min)	60
d_{33} (pC/N)	-24 to -30
Remanent polarization (mC/m^2)	80
Coercive field (V/µm)	45
Dielectric Strength ((V/µm)	400
Poling field (V/µm)	100
Transmittance (%)	>96
Clevios P Jet CEO 3	
Annealing T (ºC)	80 to 130
Conductivity (S/cm)	43
Solid content (%)	1
Viscosity (mPa.s)	7
Surface tension (mN/m)	26.9

3.1.3 Printing equipment

Two printing technologies were used to fabricate the sensors. Electrodes were printed using the inkjet printer Dimatix 2831. This printer is shown in Figure 17, and the printing process using this technology is illustrated in Figure 18. First, the printing patterns could be designed either using the printer software or using an alternative software to design a bitmap file with the desired resolution. In this work, printing patterns were designed using the software Corel PaintShop Pro X8. Secondly, a 10 pL cartridge with 16 nozzles was filled with PEDOT:PSS ink, and stored in a water-saturated atmosphere based on the ink manufacturer recommendations. Next, cartridge settings were set through the printer software. Printing settings such as substrate thickness, platen temperature, and cartridge print height were also adjusted using the printer software. The cartridge print

height and platen temperature were set to 1 mm and 38 ºC, respectively. The same parameters were used in all the experiments where the inkjet printer was used. Moreover, the printing file was loaded into the printer software. Finally, glass substrates were placed on the printer platen, and the patterns were printed.

Figure 17. *Dimatix 2831 inkjet printer.*

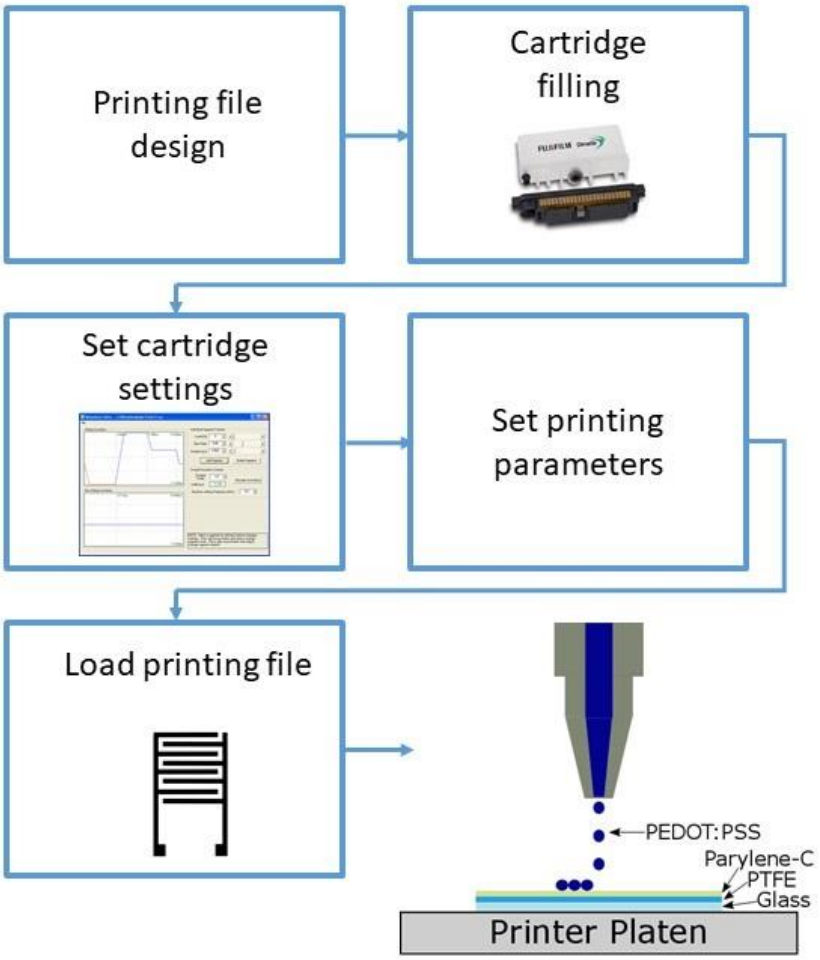

Figure 18. *Inkjet printing process diagram.*

Secondly, the screen-printing method was used to print the piezoelectric active layer of the sensors. The screen-printing machine utilized in this work was the semi-automatic TIC SCF 300 DE from Eickmeyer. This screen printer is shown in Figure 19. Printing parameters, such as screen mask height, squeegee´s distance to the screen mask, and alignment of the screen mask were adjusted manually. The screen type used was the UX 100-040/255, their properties are listed in Table 5. The screen mask can be seen in Figure 19.

Table 5. *Screen UX 100-040/255 parameters.*

Screen mask properties	
Mesh count (/cm)	100
Thread diameter (µm)	40
Mesh opening (µm)	56
Open area (%)	32

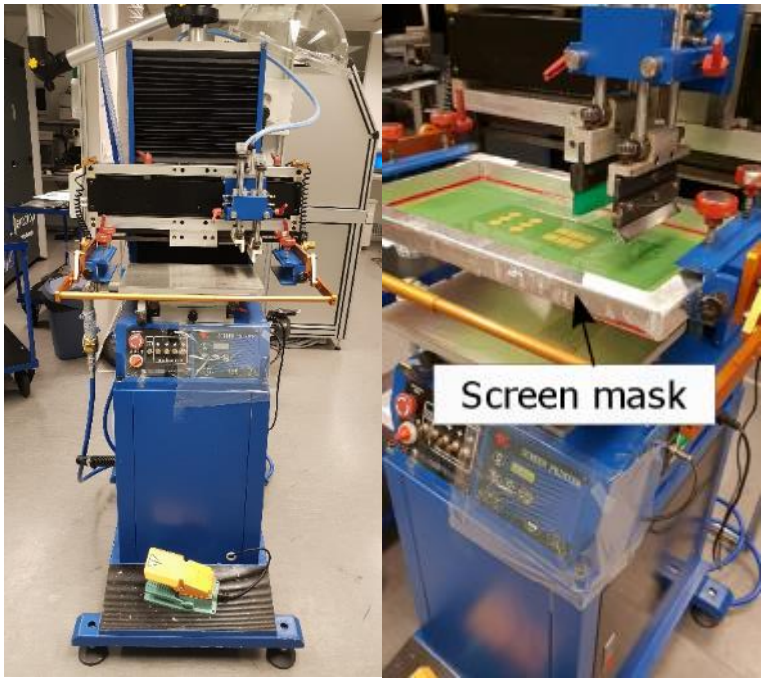

Figure 19. *TIC SCF 300 DE screen-printer.*

3.1.4 Surface treatment equipment

The surface cleaner series PSD-UV from Novascan, which is depicted in Figure 20, was used for applying UV/O_3 treatment to the substrates. Samples were placed on the sample stage inside the device chamber, and the required surface treatment time was adjusted as required using the control panel. The UV/O_3 treatment was executed under cleanroom conditions.

Figure 20. *Novascan PSD-UV surface cleaner.*

UV/O_3 is a method used to modify the surface properties of a material. When applying this treatment to polymeric materials, an oxide layer on top of the material surface is created. This process makes the surface more hydrophilic. The operating principle of this technique is based on the combination of ultraviolet light with oxygen. Ultraviolet light with two different wavelengths, 185 nm, and 254 nm, is applied to the substrate. When the 185 nm light is absorbed by oxygen, ozone is generated. The 254 nm ultraviolet light stimulates the organic molecules present in the material surface. Furthermore, the 254 nm light produces free radicals that react with oxygen. This effect generates more oxygen-containing species, which augment the surface free energy and decreases the hydrophobicity [63].

3.1.5 Poling setup

To activate the piezoelectric properties of the P(VDF-TrFE) material, a poling process was executed. The poling setup was composed of three equipment: a waveform generator, a high voltage amplifier, and an oscilloscope. Figure 21 illustrates the used equipment. The waveform generator 33500B from Keysight was used to generate an arbitrary sinusoidal waveform. This signal was applied to a high voltage amplifier, model 610C from TREK. Then, the output signal was applied to the electrodes. The applied poling field had a frequency of 50 mHz and a maximum amplitude of 10kV. Moreover, an oscilloscope DSOX2002A from Keysight was used to monitor the high voltage amplifier output signal.

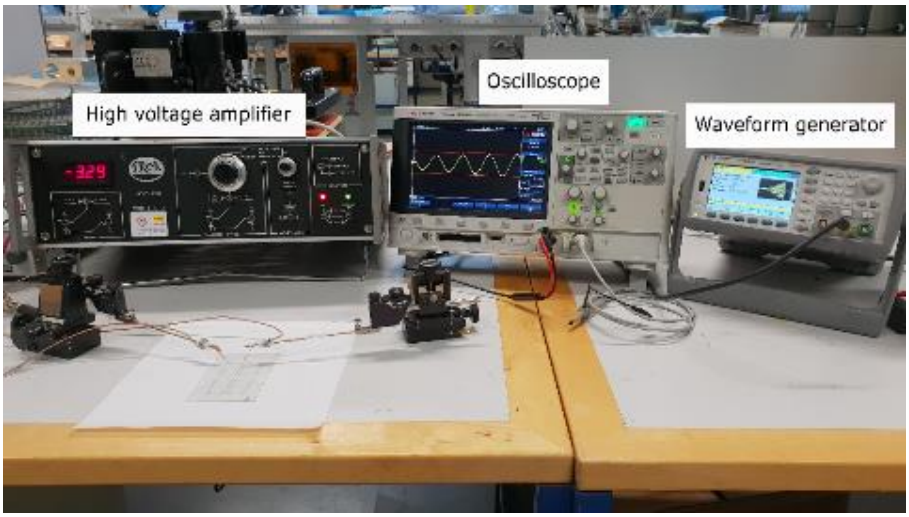

Figure 21. *Poling setup.*

3.2 Characterization equipment

All the characterization setups used in this thesis work are explained in this section. First, the electrical measurement setup is described. Then, the equipment used for inspecting the printing quality of the samples are explained. In addition, the piezoelectric sensitivity measurement setup is described.

3.2.1 Optical inspection

Printed patterns can be non-uniform due to surface energy differences of the substrate. In addition, inkjet-printed patterns can be affected by variations of the printer jetting while the printing process is being executed. Therefore, pattern dimensions can be slightly different from one sample to others during the fabrication process. Therefore, to examine the variations on the printed samples during the fabrication process, samples were inspected using an optical microscope. Moreover, the optical microscope was also used for measuring the line width of the printed patterns, and the dimensions of the final samples. The microscope used for the optical inspection of the samples was the Olympus BX51. The magnification of the microscope can be adjusted to 5X, 10X, 20X, 50X and 100X. Further, image acquisition was controlled by computer software.

In addition, a stylus profilometer was used to examine the thickness of the samples. The equipment used for performing these measurements was the Dektak XT from Bruker. The measurements were controlled through the computer software Vision64. Measurement parameters, such as stylus force, resolution, and measurement length, can also be adjusted through this software.

3.2.2 Electrical measurements setup

The electrical characterization was done using a Keysight probe station setup. Figure 22 shows this measurement setup. This setup is composed of the Keysight B1500A semiconductor device parameter analyzer. The Keysight B1500A device provides a broad variety of measurement capabilities. For instance, it is possible to measure the resistance and capacitance of a sample using the same setup. The semiconductor device parameter analyzer is controlled using the computer software Keysight EasyEXPERT. The required measurement mode can be adjusted through this software. In addition, this setup is composed of a stage where samples are placed, and the probes connected to the signal acquisition module.

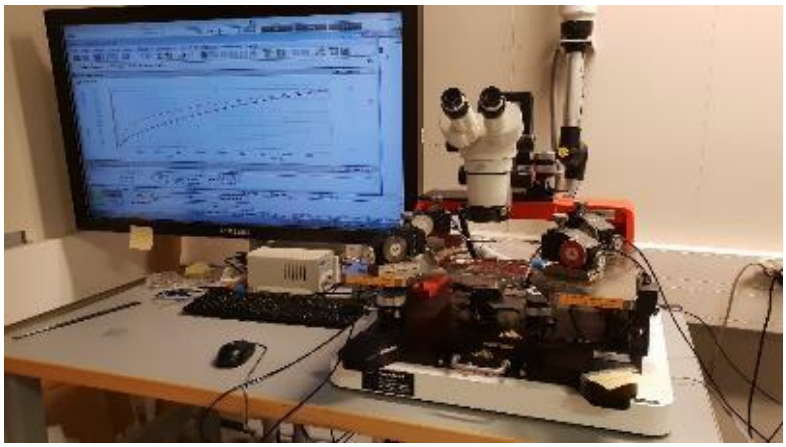

Figure 22. *Keysight probe station setup.*

3.2.3 Piezoelectric sensitivity setup

The measurement setup shown in Figure 23 was used to determine the piezoelectric sensitivity of the sensors. This device has an electrodynamic shaker with a piston that applies a dynamic excitation force to the sample when it is on the sample holder. The excitation force was controlled by applying a sinusoidal signal of 5 Hz to the electrodynamic shaker. In addition, a static force of approximately 3 N was applied to avoid the displacement of the sample while the measurement was being executed. The static force was adjusted by pressing the sample against the piston using the adjustment knobs.

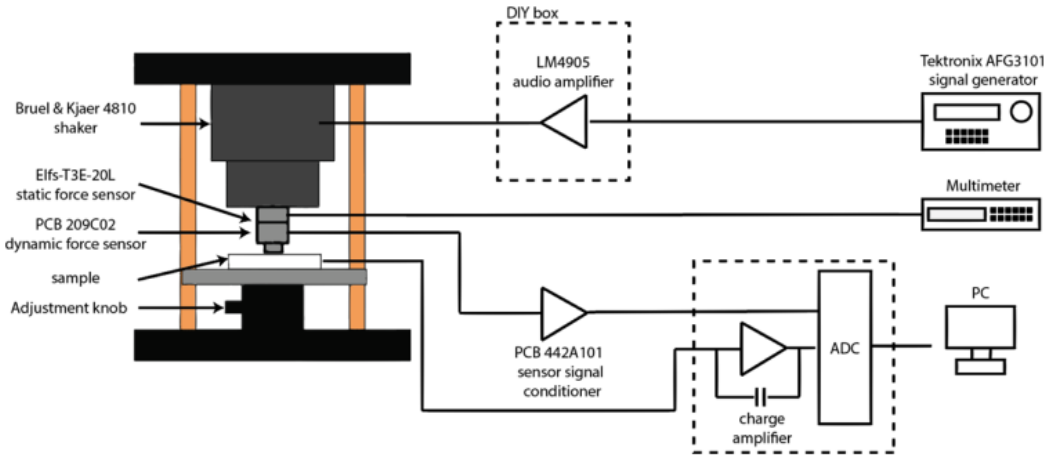

Figure 23. *Sensitivity measurement setup [64].*

As can be seen in Figure 23, the charge produced by the sample was measured using a charge amplifier and a 16-bit analog-to-digital (AD) converter. These components were connected to a PC to analyze the sensor signal. Further, voltage signals from the reference sensors were sampled with the AD converter, and the sample signal was also acquired using this module. Then, the signals were processed using MATLAB. The sensitivity was calculated as the sensor charge divided by the dynamic force that was applied to the sensor [64].

3.3 Methods

To design the IDE sensor structure, it was necessary to perform a set of experiments. The experiments were executed to analyze printing dimensions and to characterize the electrical properties of the conductive material. Experiment results were used to design electrodes printing pattern.

3.3.1 Printing test

The first step was to test if it was possible to print uniform PEDOT:PSS lines on Parylene-C. By doing this test, it was observed that the printed patterns were not uniform. This was because of the hydrophobic properties of the substrate material. Hydrophobic materials are characterized by repelling polar liquids (e.g. water) easily, and the selected conductive material ink is water-based. Then, the next step was to find a suitable surface treatment to make the Parylene-C substrate hydrophilic. From the literature review, it was found some methods that can be used to change hydrophobic surfaces into hydrophilic, such as oxygen plasma, chemical grafting, and UV/O_3. Of these methods, the most practical is UV/O_3 as it requires less sophisticated processes, and it offers minimal

hydrophobic recovery. Further, this treatment method also has as an advantage that it can be executed under atmospheric pressure, and therefore the equipment costs are reasonably low [63][65]. Therefore, it was necessary to analyze the effect of the UV/O_3 treatment on the wetting properties of Parylene-C used in this research.

The next performed experiment was to analyze the effect of the UV/O_3 treatment on the substrate and to find a suitable drop spacing to form uniform and thin lines. The experiment was executed by varying two parameters, surface treatment time and drop spacing. All the analyzed test cases are listed in Table 6. In each sample, a drop matrix was printed to measure the drop size. Five random droplets from the matrix were selected and measured. The drop size was measured using an optical microscope using a magnification of 20X. Then, the mean value of the five measurements was calculated to obtain an approximate value of the drop size. Moreover, a set of five parallel lines was printed to measure the line width. The lines to be printed were designed to be only one-pixel width to obtain the smallest line width after printing. Once the lines were printed, it was used an optical microscope to check the print quality and to measure the line width for each test case. Line width was also measured using an optical microscope with a magnification of 20X. The average value of the line width was calculated based on ten measurements taken from random line places. These experiments were necessary to do to find the optimal drop spacing and the optimal substrate treatment time.

Table 6. *Test cases based on surface treatment time and drop spacing variations.*

Test Case	Surface Treatment Time	Drop Spacing (µm)
1	5	45
2	5	50
3	5	55
4	5	60
5	5	65
6	10	45
7	10	50
8	10	55
9	10	60
10	10	65
11	15	45
12	15	50
13	15	55
14	15	60
15	15	65
16	25	45
17	25	50
18	25	55
19	25	60
20	25	65
21	35	45
22	35	50
23	35	55
24	35	60
25	35	65
26	45	45
27	45	50
28	45	55
29	45	60
30	45	65

3.3.2 Edge roughness measurements

This experiment was done to analyze the effect of the drop spacing on the edge roughness along the edges of printed lines. The line edge roughness can be defined as the deviation of the edge from a uniform and ideal shape. To perform this analysis, two random lines were selected from each test case detailed in Table 6. Thus, ten measurements were taken from each line. Measurements were taken using an optical microscope with a magnification of 20X. Then, a statistical analysis was done to determine the line

edge roughness. Additionally, the minimum line distance was determined based on the line width variation. Results of the line edge roughness analysis are presented in chapter 4.

3.3.3 Conductive ink characterization

After finding a suitable drop spacing, it was necessary to characterize the electrical properties of the ink. The first thing to do was to measure the material sheet resistance. Subsequently, its conductivity was calculated. First, the four-point probe method was used to perform the resistance measurement. However, it was observed that the ink exhibited a very high resistance by using this method. Therefore, it was not possible to obtain a resistance value with the measurement equipment due to its limited range. The measurement device was the Keithley 2425 sourcemeter, and the material resistance was out of the device range.

Secondly, to improve the conductivity of the printed pattern, it was tried to print multiple layer lines as well as multiple layer pads. The first layer was printed based on the optimal drop spacing, and the subsequent layers were printed using a smaller drop spacing. The results of this experiment showed that it was possible to print a big pad using multiple layers, but it was not possible to print multiple layer lines. Lines printed using the multilayer method are shown in Figure 24. From the image in Figure 24a, it can be seen that the printing of two-layer lines was done successfully. However, different results were obtained when the same process was repeated. Figure 24b shows printed lines using the same printing parameters as in Figure 24a. The challenges faced in this experiment were due to the inkjet printer resolution. Furthermore, the spreading of the ink could be affected by differences in the surface energy of the substrate. Therefore, it was needed to execute the experiment using a different approach.

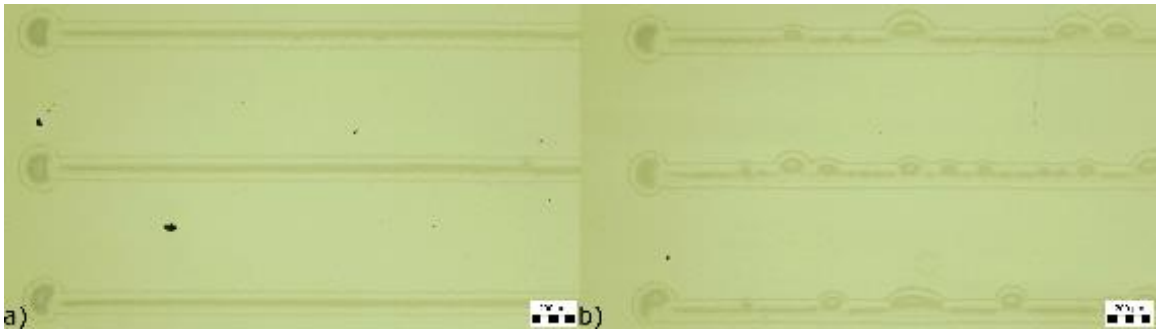

Figure 24. *Two layers lines printed under the same conditions: a) uniform line; b) defects on the printed line.*

Next, a new pattern was printed to perform the 2-point probes measurement. The pattern used in this experiment is shown in Figure 25. The whole structure was printed using PEDOT:PSS ink. The pattern was printed as follows. First, the lines were printed using the same resolution and dimensions as the ones to be used in the IDE structure design. Next, pads were printed using the multi-layer approach. Although better results were obtained in this experiment, the resistance was still too low compared to the manufacturer specifications.

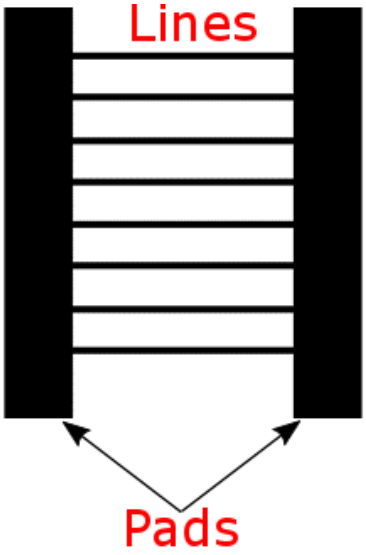

Figure 25. *Resistance test pattern.*

Thus, it was decided to analyze the annealing temperature effect on the PEDOT:SS conductivity. According to the manufacturer specifications, the recommended annealing conditions were between 80 ºC to 130 ºC for 15 minutes. The pattern used in the previous experiment was printed again, but the annealing conditions were varied. The test cases analyzed in this experiment are detailed in Table 7.

Table 7. *List of parameters for the conductivity test.*

Time (min)	Annealing Temperature (°C)
15	90
15	110
15	130

Finally, sheet resistance was calculated as follows. The equivalent resistance of the 8 lines printed in parallel was measured using the Keysight probe station setup. Thus, as there were 8 lines in parallel in the measurement pattern, the equivalent resistance R_T value can be expressed by equation (17).

$$\frac{1}{R_T} = \frac{1}{R_1} + \frac{1}{R_2} + \cdots + \frac{1}{R_8} = \frac{8}{R_1} \tag{17}$$

Then, it was possible to calculate the resistance of each line (R) based on the equivalent resistance. Subsequently, the sheet resistance R_S can be calculated using equation (19), where L corresponds to the line length, w to the line width, and t to the line thickness. Based on the initial tests, it was observed that the line thickness of the printed lines was not uniform. Thus, it was used the mean value of the line thickness measurements to calculate the material conductivity. Equation (20) was used to calculate the conductivity.

$$R = \rho \cdot \frac{L}{w \cdot t} = R_S \frac{L}{w} \tag{18}$$

$$R_S = \frac{R \cdot w}{L} = \frac{\rho}{t} \tag{19}$$

$$\sigma = \frac{1}{\rho} \tag{20}$$

3.4 Sensor pattern design

The sensor dimensions were mainly designed based on the results of the experiments of section 3.3.1 and 3.3.2. To avoid short-circuit between the electrodes, it was decided to set the distance between the fingers center equal to the finger width plus four times the standard deviation of the finger width. The finger width was set based on the line roughness experiment. Thus, IDE fingers were designed to be one pixel width. The resulting number of fingers using those dimensions was 80. IDE structure and sensor dimensions are depicted in 0. This figure shows the dimensions based on the printing file design. However, real dimensions differ from the design because the ink will spread on the substrate giving a higher line width.

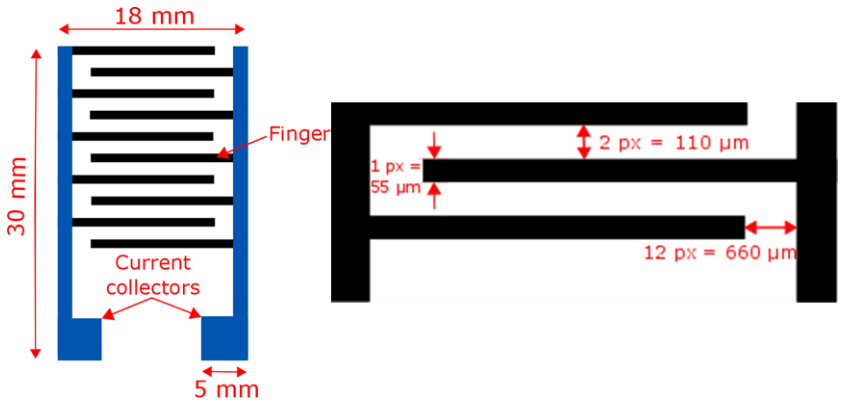

Figure 26. *IDE sensor dimensions.*

The next step was to design the printing file of the sensor structure. The drop spacing used for printing the IDE fingers was higher than the one used for printing the current collectors. Therefore, two printing files were designed. Figure 27 shows the design of the printing files. The patterns shown in Figure 27a and Figure 27b were designed to print the current collectors and the electrode fingers, respectively. A more detailed description of the printing process of the sensor structure is given in section 3.5.

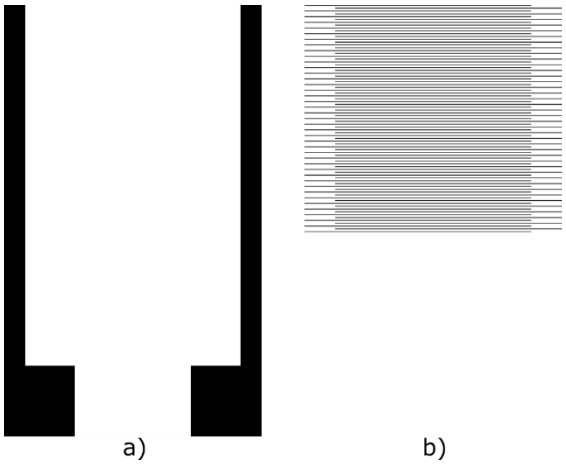

Figure 27. *IDE printing patterns: a) current collectors; b) IDE fingers.*

3.5 Sensor fabrication

A set of 12 samples were fabricated in cleanroom conditions. The fabrication process of the final samples is depicted in Figure 28. First, glass substrates were cleaned to improve printing quality. Subsequently, they were spin-coated with PTFE. Then, the substrates were annealed at 100 °C for 10 min and at 150 °C for 30 min. Next, a Parylene-C layer with an approximated thickness of 2 µm was deposited on top of the glass carriers. The next step was to place the substrates in the UV/O_3 chamber for 10 minutes to make the Parylene-C layer hydrophilic. After these substrate preparation steps, substrates were prepared to start printing the sensor layers.

IDE patterns were inkjet printed using PEDOT:PSS ink. To print the electrodes, the process was divided into 2 main steps. First, fingers were printed using a drop spacing of 55 µm. Then, current collectors were printed using the multilayer approach. In total, 6 layers were printed; the first layer was printed using a drop spacing of 40 µm, and the following layers were printed using a drop spacing of 20 µm. Samples were annealed at 130 °C for 15 minutes to make the material conductive. Once the electrodes were fabricated, the P(VDF-TrFE) layer was screen printed on top of them. After printing the piezoelectric active layer, samples were annealed at 135 °C for 1 hour. Once the printing

processes were completed, the piezoelectric material was poled using the setup described in section 3.1.5.

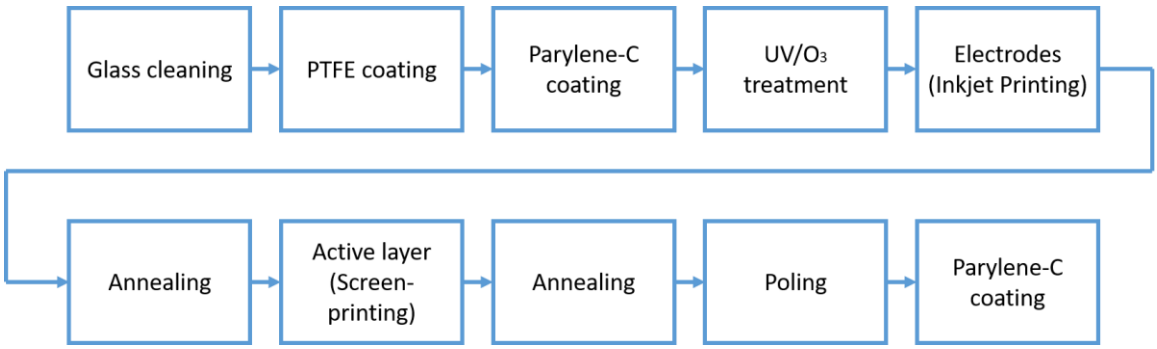

Figure 28. *Sensor fabrication process.*

After all the samples were poled, it was necessary to attach some connectors to the sensors. Thin cables were attached to the pads of the samples using a screen printable PEDOT:PSS ink. Then, the samples were annealed at 90 °C per one hour. Further, the second layer of Parylene-C was coated on top of the sensors to prevent electrodes degradation. The thickness of this layer was about 1 µm. Finally, sensors were peeled off from the glass carriers and attached to a polyethylene terephthalate (PET) foil. Some pictures of the final samples are illustrated in Figure 29. It can be seen the samples after peeling them off from the glass carrier, and a sensor attached to the skin.

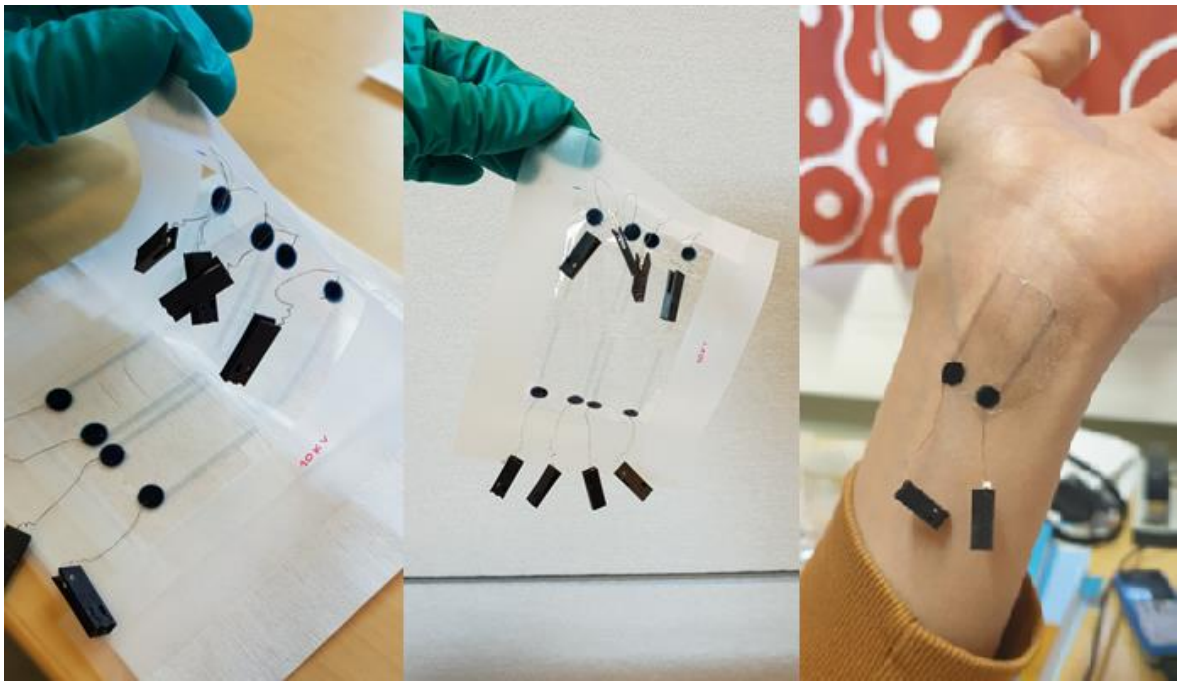

Figure 29. *Final samples pictures.*

3.6 Sensor characterization

During the whole fabrication process, samples were inspected to check printing quality after each printing step. In addition, electrical properties were also characterized. Resistance was measured after each printing step to control the resistance variation. Once all the samples were finished, resistance and capacitance were measured. Further, the piezoelectric sensitivity of the samples was measured. The processes used to characterize the samples are detailed next.

3.6.1 Print quality

Samples were inspected using an optical microscope. IDE structure dimensions were measured after annealing the printed patterns. Moreover, the optical microscope was used to check the print quality. This was also done to detect print-quality defects that could create short-circuit between the electrodes.

In addition, the thickness of the samples was also examined using the stylus profilometer described in subsection 3.2.1. Measurements were done only to three samples. Thickness was measured in five different places for each sample. The measurements represented the average thickness of the electrodes layer plus the P(VDF-TrFE) layer. Thus, the average thickness of each sample was calculated based on the five measurements. Furthermore, a single printed P(VDF-TrFE) layer was measured to have a reference of the thickness of the active layer.

3.6.2 Electrical characterization

Resistance and capacitance were measured for a set of 10 samples. The setup explained in section 3.2.2 was used to perform these measurements. Resistance was measured after printing and annealing the IDE structure to detect possible short-circuits between the electrode fingers and to determine if the leakage current could prevent the poling of the device. In addition, the resistance of the final samples was also measured. The method used to measure the resistance was the 2-point probe measurement. Measurements were executed before peeling the samples off from the glass carriers. First, probes were connected directly to the sensor pads before printing the active layer. Figure 30 shows probe connections. Lastly, when the samples were finished, probes were connected to the sensor connectors as can be seen in Figure 31. Capacitance was measured after all the fabrication processes were completed.

Figure 30. *Probes connection before printing the active layer.*

Figure 31. *Probes connection to the final samples.*

3.6.3 Piezoelectric sensitivity measurements

The piezoelectric normal and bending mode sensitivity were measured for all the samples using the setup described in section 3.2.3. Measurements were done for each sample in ten different places in both cases. The piezoelectric normal mode sensitivity was determined by performing the measurement while the samples were still attached to the glass carrier. In this case, the samples were placed on the sample holder (Figure 32a), and a piece of PET foil was placed between the sample and the metallic piston to avoid short-circuit. In this scenario, the results should not be affected by any bending. Furthermore, bending mode sensitivity was determined by placing the samples on a PET foil after peeling them off from the glass carrier. Then, the sample under test was placed on a PDMS holder with a small hole in the center such that the active part of the sensor was

on top of the hole (Figure 32b). By using this setup, when the piston was applying an excitation force to the samples, the samples were bent.

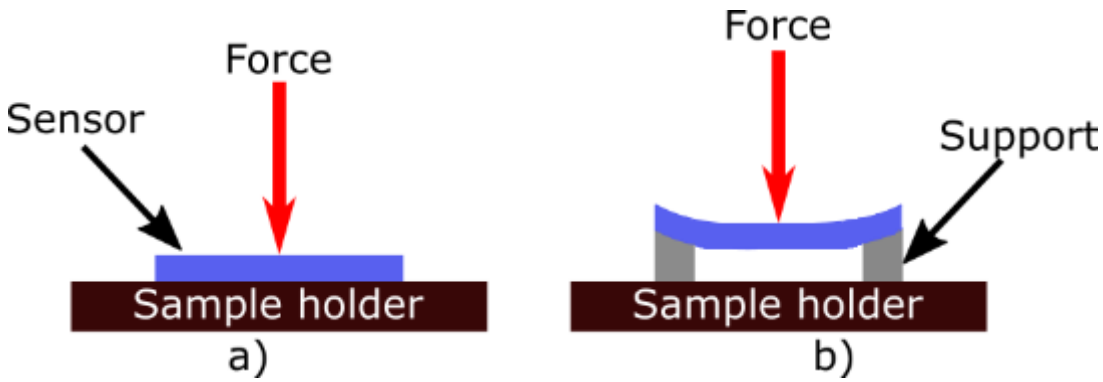

Figure 32. *Piezoelectric sensitivity measurement modes: a) normal mode; b) bending mode.*

4. RESULTS

In this section, all the experiment outcomes are summarized. Moreover, the results obtained when characterizing the final samples are presented. First, printing experiments to evaluate substrate wettability are detailed. In addition, the characterization of printed lines is also analyzed. Then, conductive ink characterization results analysis is presented. Finally, an analysis of the electrical and piezoelectric properties of the final samples is given.

4.1 Surface treatment optimization

All the experiments done before the fabrication of the final samples were based on inkjet printing technology. The results and analysis of these experiments are presented in this section. First, substrate wettability is evaluated. Then, an analysis of the line width variation based on the printing resolution and surface treatment time is given.

At the beginning of the experiments, printed lines on Parylene-C revealed that the substrate was highly hydrophobic. As explained in section 3.3.1, UV/O_3 surface treatment was used to improve the wetting properties of the ink on the substrate surface. Figure 33 shows the drop diameter variation based on different exposure times. The drop size increased for all the exposure time analyzed in this experiment. Based on these results, it can be concluded that UV/O_3 treatment effectively changed the surface properties by increasing its hydrophilicity. Furthermore, it was observed that it was enough to treat the substrate for 5 minutes to increase the drop size. An increase in the drop size was also detected in the next three test cases (10, 15, and 20 minutes). However, when the exposure time was higher than 30 minutes, the drop size started to decrease. This could happen due to substrate material degradation.

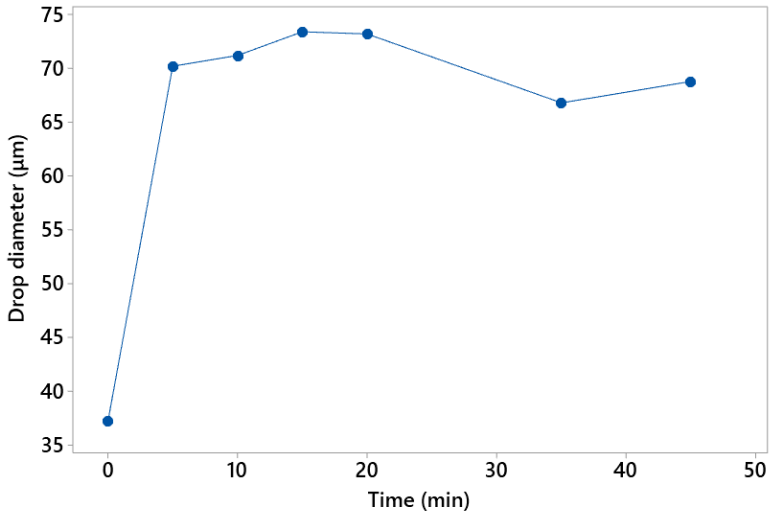

Figure 33. *Drop diameter variation for different drop spacing and different UV/O_3 exposure time.*

Furthermore, the wetting properties of a material or surface are usually determined by measuring the contact angle. The contact angle is determined as the angle created by the intersection of the liquid-solid interface and the liquid-vapor interface. The wetting of the liquid on the substrate is high when the contact angle is << 90°. In contrast, when the contact angle is >> 90°, the wetting is unfavorable [66]. The contact angle variation also results in a variation in the drop size. The smaller the contact angle, the higher the drop size is, and vice versa. Thus, these can also be an alternative method to characterize the wetting properties of a substrate. A literature survey was done to find any reported study about the relation between the contact angle and drop size of liquids deposited on UV/O_3 treated Parylene-C. However, it has not been reported any study about the effect of UV/O_3 on Parylene-C. On the other hand, it has been reported that applying oxygen-plasma treatment to the Parylene-C substrate the material turns hydrophilic [67][68]. Therefore, UV/O_3 treatment could be an alternative method to improve Parylene-C wettability. Although alternative approaches to investigate the wetting properties exist, it was demonstrated that measuring the drop size is a simple process to determine if the wetting properties of a material have been changed.

Next, the analysis of the line width variation was done based on different drop spacing and different UV/O_3 exposure time. This experiment was done to examine how to control the width of the fingers that would be used in the IDE structure. Furthermore, this was needed to do because the finger width variation has an impact on the total capacitance of the IDE sensor. IDE sensors with narrow fingers exhibit a lower capacitance value compared to electrodes with wider fingers [69]. This results in a higher output voltage. Figure 34 shows the interval plot of the analyzed groups. The interval plot illustrates a

95 % confidence interval for the mean of each test case. The confidence interval represents the range of values where the population mean could be included. Moreover, the mean value of each test case is also represented.

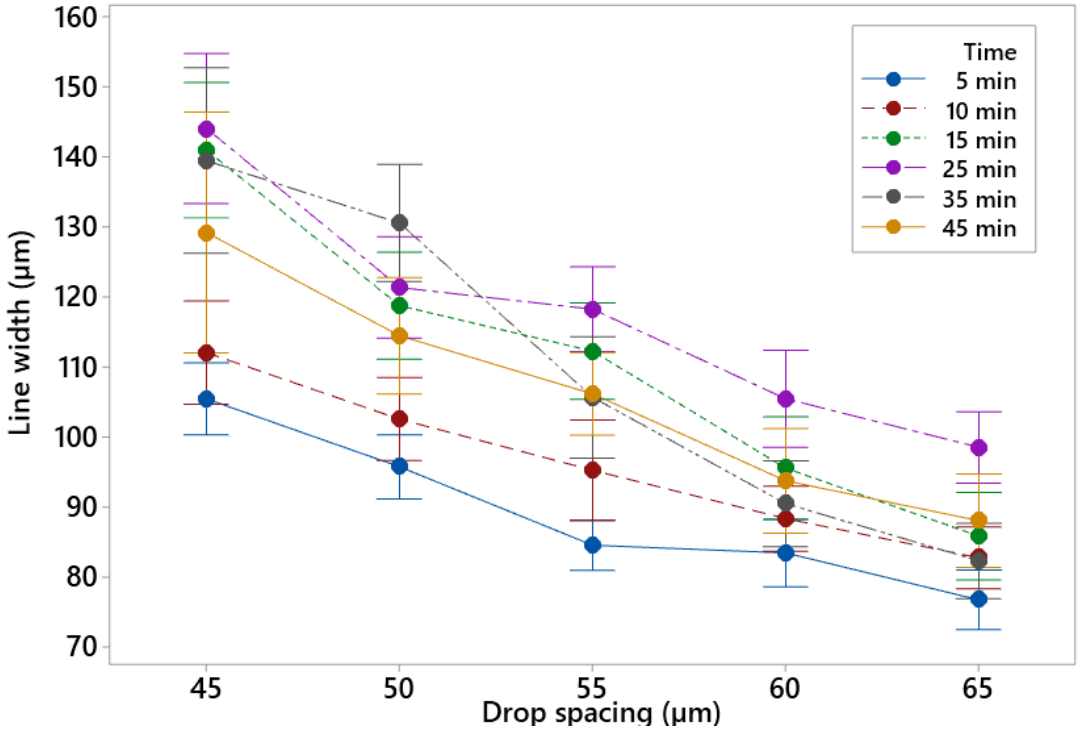

Figure 34. *Interval plot of the line width variation for different drop spacing and different UV/O_3 exposure time.*

What can be seen in Figure 34 is the impact of the drop spacing on the line width. In all the cases, wider lines were observed when a smaller drop spacing was used, while narrower lines were observed using a higher drop spacing. Additionally, the line morphology of the printed lines was also affected by the drop spacing. Although the lines did not show any discontinuity, the lines were not uniform in all cases. For example, lines printed with a drop spacing of 65 µm showed scalloping along the line edge. The uniformity of the lines is mostly influenced by the drop spacing and the delay period between droplets deposition. In general, five morphologies can be seen in printed lines. When the drop spacing is higher than the drop diameter, individual drops are formed. Then, when the drop spacing is decreased drops start to merge and scalloped lines are created. Uniform lines are created by further decreasing the drop spacing. However, if the drop spacing is very small, a bulging line is generated. Moreover, if the evaporation of a droplet occurs in a small period time than the jetting period, individual drops will dry forming a stacked coin pattern [70].

Additionally, the motivation of this experiment was to examine the effect of drop spacing and surface treatment time on the line width. First, the effect of surface treatment time was analyzed. As can be seen from Figure 34 narrower lines were printed when the substrate was UV/O_3 treated for 5 and 10 minutes. In addition, when the substrate was treated for 15 and 25 minutes, lines were wider for all the drop spacing values. On the other hand, as the drop diameter decreased when the substrates were treated for 35 and 45 minutes, there was a reduction in the width of the lines. From this preliminary analysis, it could be concluded that it was enough to expose the substrate to UV/O_3 treatment for 5 or 10 minutes.

Therefore, it was observed that the variation of the line width was lower when the substrate was treated for 5 and 10 minutes, and when the lines were printed using a drop spacing of 55 µm and 60 µm. In summary, when the substrate was treated for 5 minutes, it was obtained a line width size of 82 µm and 81 µm using a drop spacing of 55 µm and 60 µm, respectively. In addition, line width was 94 µm and 85 µm when the substrate was treated for 10 minutes using a drop spacing of 55 µm and 60 µm, respectively. These four cases are illustrated in Figure 35. Based on these images, it can be seen that the line width is smaller for 5 minutes treated samples. Nevertheless, the lines are more uniform on samples treated for 10 minutes. Then, the next thing to do was to choose which surface treatment time would be used in the sensor fabrication process.

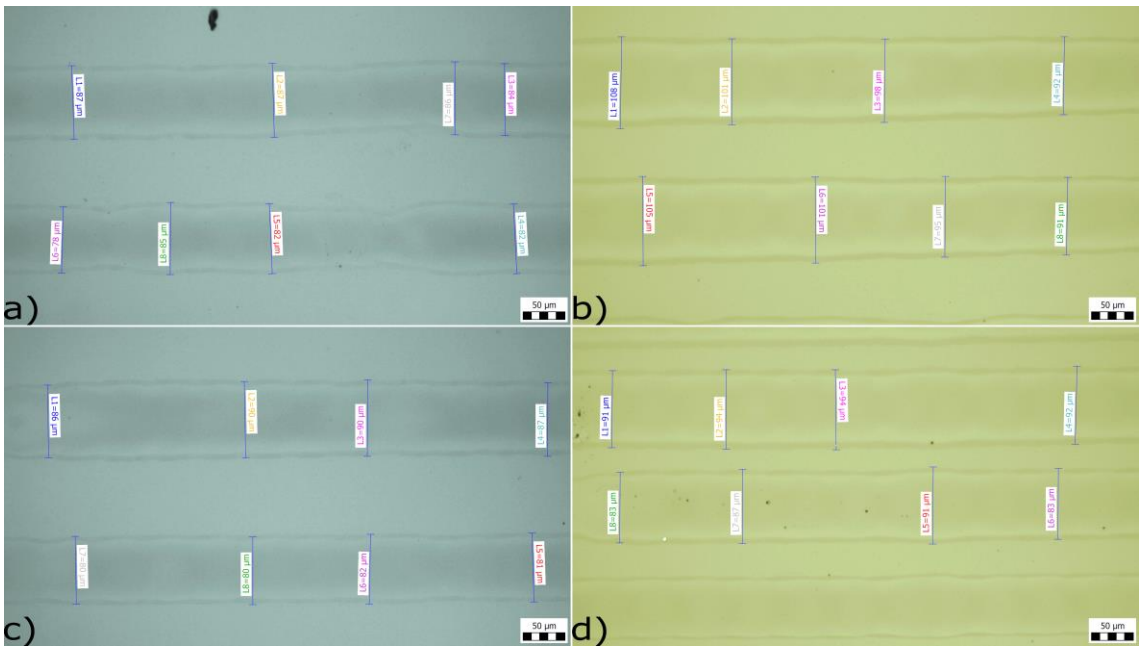

Figure 35. *Printed lines. 55 µm drop spacing: a) 5 minutes UV/O_3 treated substrate; b) 10 minutes UV/O_3 treated substrate. 60 µm drop spacing: c) 5 minutes UV/O_3 treated substrate; d) 10 minutes UV/O_3 treated substrate.*

Consequently, between 5 and 10 minutes of surface treatment time, it was chosen to use 10 minutes. This selection was done for practical reasons. Patterns printed on the substrate treated for 5 minutes were difficult to see using the printer camera after the printing process. This could be an inconvenience when it is needed to print two consecutive patterns with different drop spacing as the alignment is done by optical inspection of the first printed pattern. Therefore, the printing process variation of printed lines on 10 minutes UV/O_3 treated substrates was examined. The analysis was done for printed lines using 55 µm and 60 µm drop spacing. Some statistics parameters of the printed lines are listed in Table 8.

Table 8. *Statistics values of printed lines in 10 minutes UV/O3 treated substrate.*

Line	Mean (µm)	STD (µm)	Min. (µm)	Max. (µm)
DS55-1	95.20	10.04	72	108
DS55-2	93.70	9.26	72	105
DS60-1	88.30	6.50	75	95
DS60-2	82.00	5.72	69	91

Additionally, the Two-sample T-test was used to verify if the differences of the means of the line widths were significant to determine line-to-line variation (i.e. printing process variation). In this case, lines printed with the same drop spacing were compared. The test results are presented in Table 9. The parameter listed in the third column represents the difference between the population means. The 95% confidence interval provides an estimated range where the difference could be included. Furthermore, the P-value is used to determine if the difference between the means is statistically significant. Generally, a threshold of 0.05 is used for the P-value [71]. When the P-value is less than or equal to the threshold value, the difference is statistically significant. As can be seen, the P-value is higher than the threshold when the lines were printed using a drop spacing of 55 µm, and it is below the threshold for a drop spacing of 60 µm. Thus, for a drop spacing of 55 µm, the difference between the means is not statistically significant. The results suggest that the printing of the lines can be repeated without showing a meaningful variation in the line width dimensions. However, for a drop spacing of 60 µm, it can be assumed that the line width of the printed lines is different despite using the same drop spacing.

Table 9. *Two-sample T-test, line-to-line variation.*

Population A	Population B	Difference	95% CI for Difference	P-value
DS55-1	DS55-2	1.50	-7.61 to 10.61	0.733
DS60-1	DS60-2	6.30	-0.53 to 12.07	0.034

Nonetheless, the results could be negatively affected by skewness and outliers of the sample data. Therefore, data was represented using a boxplot to examine the data distribution. Figure 36 displays the data distribution of the analyzed cases. As can be seen in Figure 36a, lines printed using 55 µm drop spacing show a similar line width. On the contrary, data distribution of lines printed using 60 µm drop spacing seems to be severely skewed as seen in Figure 36b. Comparing the data distribution for both cases, it can be seen that the line width values are distributed in the same interval when lines were printed using 55 µm drop spacing. However, lines printed using 60 µm drop spacing show a big difference between the interval distributions. Additionally, it should be noted that data distribution show outliers in both cases. Outliers represent unusual data points in a data set. These values can have an excessive effect on the mean value of the line width.

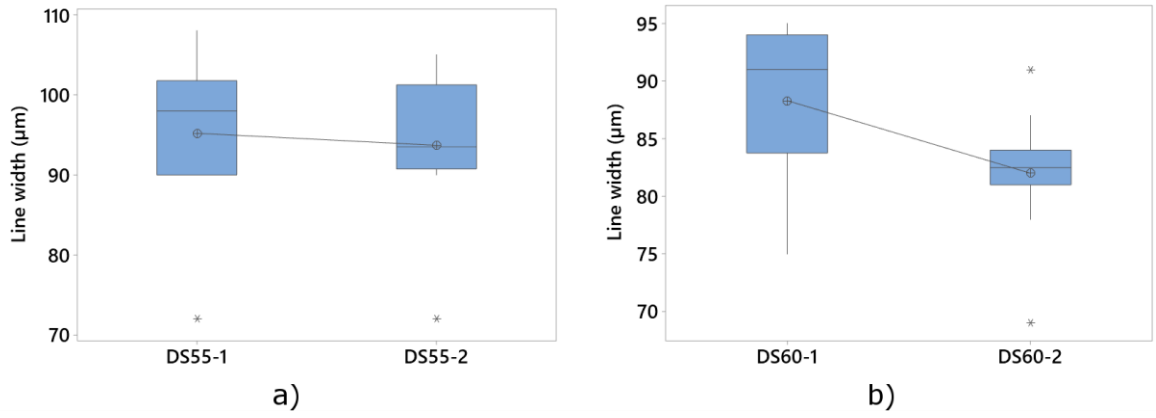

Figure 36. *Boxplot of line width measurements: a) printed lines using 55 µm drop spacing; b) printed lines using 60 µm drop spacing.*

Therefore, statistics values calculation was repeated without including the outliers. Nevertheless, data from lines printed using 60 µm drop spacing was not analyzed because of the considerable difference between the interval distributions. Thus, it was observed that although the mean value increased, the standard deviation decreased (Table 10). Consequently, it was chosen to use 55 µm drop spacing to print the fingers of the IDE structure based on the analysis results.

Table 10. *Statistics values of printed lines in 10 minutes UV/O3 treated substrate, outliers removed.*

Line	Mean (µm)	STD (µm)	Min. (µm)	Max. (µm)
DS55-1	97.78	6.22	90	108
DS55-2	96.11	5.58	90	105

4.2 Line edge roughness

Printing quality can be affected by the surface properties, drop spacing, and ink properties. The objective of this thesis work was to develop a printed piezoelectric sensor based on IDE structure which can be poled with the available 10 kV high voltage amplifier. Thus, before designing the IDE dimensions, it was necessary to examine the limitations of the printed lines based on the printing quality. For example, if the edge roughness of the line is too high, there will be short-circuits between electrodes which will lead to failure of the device. In addition, the distance between fingers should have a minimum distance gap to avoid the electrical breakdown of the piezoelectric material during the poling process. Thus, this analysis was done to find the optimal drop spacing to minimize the edge roughness of the electrode fingers. The minimal edge roughness allows the placement of the electrodes as close to each other as possible. This, in turn, allows maximum design variability in the IDE structure.

The relationship between the standard deviation of the measured line widths (i.e. the edge roughness) and drop spacing and substrate treatment time is represented in a contour plot (Figure 37). This plot is a graphical representation of a three-dimensional (3D) surface on a two-dimensional (2D) plane. Therefore, the points in the same range are represented using a specific color. As can be seen in the graph, higher edge roughness are on the left side of the plot which corresponds with small drop spacing values. Furthermore, this occurs when the substrate has been treated from 10 to 45 minutes. On the other hand, lower values of edge roughness are on the right side of the plot which corresponds to higher drop spacing values, and the same results are obtained for almost all surface treatment times. However, there are small regions where the edge roughness is higher than expected.

Therefore, based on the contour plot graph, the chosen surface treatment time and drop spacing (i.e. 10 minutes and 55 µm) do not show the lowest standard deviation. Nevertheless, it should be noted that the contour plot representation was done only using the data of one printed line of each test case, and the representation of the results could be biased. Therefore, a higher number of data points should be used to avoid a high variability between the analyzed cases.

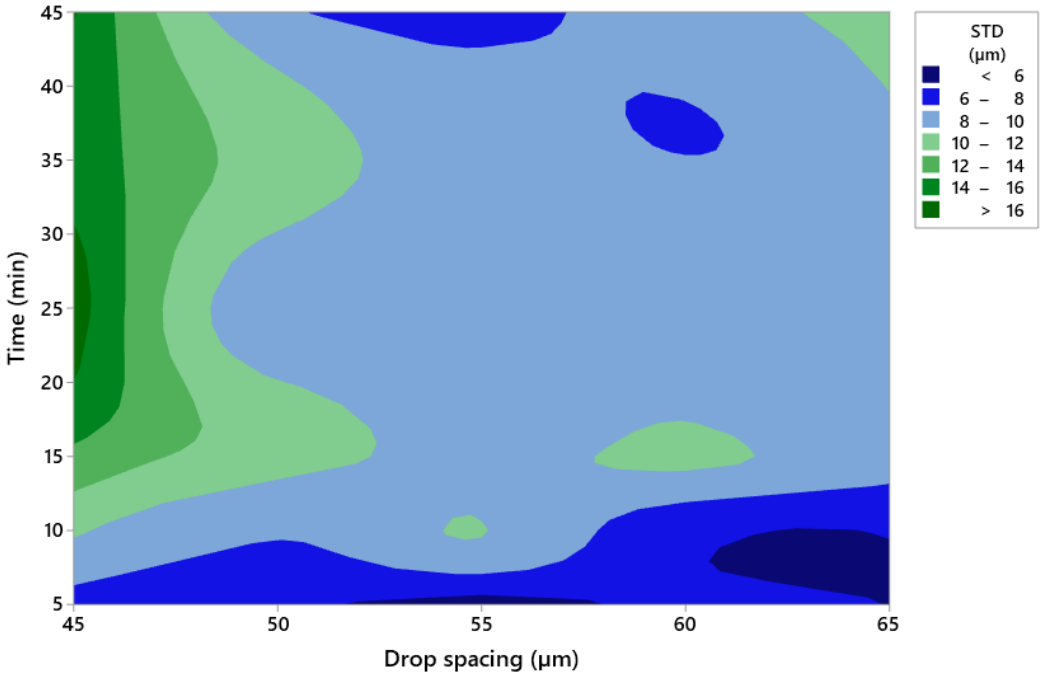

Figure 37. *Contour plot of line width standard deviation vs. surface treatment time and drop spacing.*

4.3 PEDOT:PSS electrical characterization

As was explained in section 3.3.3, the electrical properties of the conductive ink were analyzed by measuring the equivalent resistance of 8 lines printed in parallel. Thus, to calculate the sheet resistance of the material, it was necessary to measure the thickness of the printed lines. Therefore, the line profile was characterized to examine the PEDOT:PSS material distribution. Figure 38 illustrates the PEDOT:PSS distribution of a printed line. From this analysis, it was observed the coffee-ring effect on the material distribution. This phenomenon is produced because of the solvent evaporation which leads to differences in the temperature resulting in higher concentrations of the particles in comparison with the center of the printed drop [72]. Furthermore, this effect is typically seen when the ink is deposited onto materials with high surface energy.

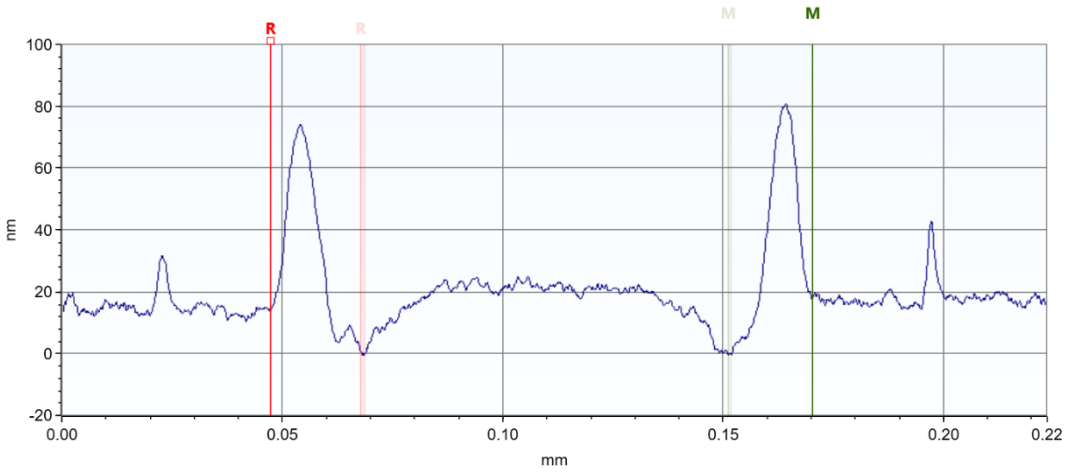

Figure 38. *Line profile of a printed line using 55-µm drop spacing.*

Consequently, to determine the sheet resistance of each line, the following procedure was followed. First, line resistance was calculated using the equation (17). Then, equation (19) was used to determine the material sheet resistance. As the line thickness was not uniform, it was used the mean value thickness. The line width was estimated based on the measurements that were done using the microscope. Thus, both values were used to compute the cross-section area of the printed lines, and subsequently the material conductivity. The conductivity of the material was also examined by varying the annealing temperature. The sheet resistance and the conductivity of the material for different annealing temperatures are listed in Table 11. Nevertheless, the conductivity was very poor for all the test cases. The results were very low in comparison to the manufacturer specification which was 43 S/cm. In summary, higher conductivity was obtained when the printed lines were annealed at 130 ºC for 15 minutes. Nonetheless, it should be noted that the determined effective conductivity was used only as a reference. As the conductive material is mainly distributed on the line edges, the material conductivity may be calculated more accurately using the dimensions of the region where the PEDOT:PSS material is spread (i.e. area and length).

Table 11. *PEDOT:PSS ink properties for different annealing temperatures.*

Annealing T	Sheet Resistance (MΩ/sq)	Eff. conductivity (mS/cm)
90 ºC	127.70	3.58
110 ºC	35.78	11.49
130 ºC	9.28	48.87

Additionally, the main issue related to the poor conductivity of the conductive material is the non-uniform thickness of the printed lines. According to the ink manufacturer specifications, the thickness of a printed pattern to exhibit high conductivity should be at least 100 nm. As can be seen in Figure 38, the concentration of the material is higher at the edges of the line but still lower than 100 nm. The effective conductive cross-sectional

area of the PEDOT:PSS conductors is therefore very low. The observed behavior can be explained by the coffee-ring effect. This phenomenon induces the segregation of the ink particles to the line edge. Several parameters can have an impact on the ink distribution. For example, ink and substrate wettability, ink viscosity, solvent type, particle size, droplet volume, and droplet drying conditions [73].

4.4 Final samples characterization

The analysis of the characterization of the final samples is presented in this section. A set of 10 samples were characterized. First, it is detailed the IDE dimensions. Then, electrical and piezoelectric sensitivity measurement results are presented.

4.4.1 IDE dimensions

First, samples were inspected using a microscope after the inkjet printing process was completed. This process was done to check if there was any defect such as short-circuits between electrodes or any discontinuity on the printed patterns. Thus, it was not observed significant printing defects. In addition, IDE structure dimensions were measured. Figure 39 shows an image of a sample where can be observed the variation of the structure dimensions. As can be seen, the distance between the right and left finger end were different. There was a variation of more than 100 µm. These values did not match with the dimensions from the designed pattern, as expected.

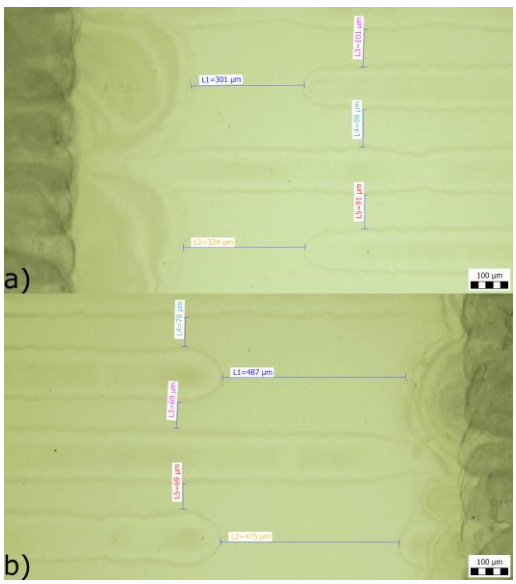

Figure 39. *Distance between current collectors and fingers: a) right side; b) left side.*

In addition, the finger width was measured to determine the variation range. An image of IDE fingers is shown in Figure 40. As can be observed in this image, the width of the fingers was not uniform. Based on the images obtained from the printed IDE structures, it was determined that the finger width varied from 100 to 130 µm. This fluctuation leads to a variation in the fingers gap. The variation of the line width corresponds to the non-uniform distribution of the ink. This occurred due to the differences in the surface energy of the substrate which affect the spreading of the ink on the substrate. In addition, ink behavior during the printing process may also have an impact on print quality. The dimensions of the IDE structure are summarized in Table 12.

Figure 40. *IDE fingers.*

Table 12. *IDE sensor dimensions.*

Dimensions (µm)	
Line width	100 to 130
Finger gap	50 to 100
Current collector distance (right)	300 to 330
Current collector distance (left)	470 to 490

In general, the printing quality was acceptable. Figure 41 shows images of the printed IDE structure. Nevertheless, the variation of the finger width and finger gap could have an impact on the capacitance of the sensors.

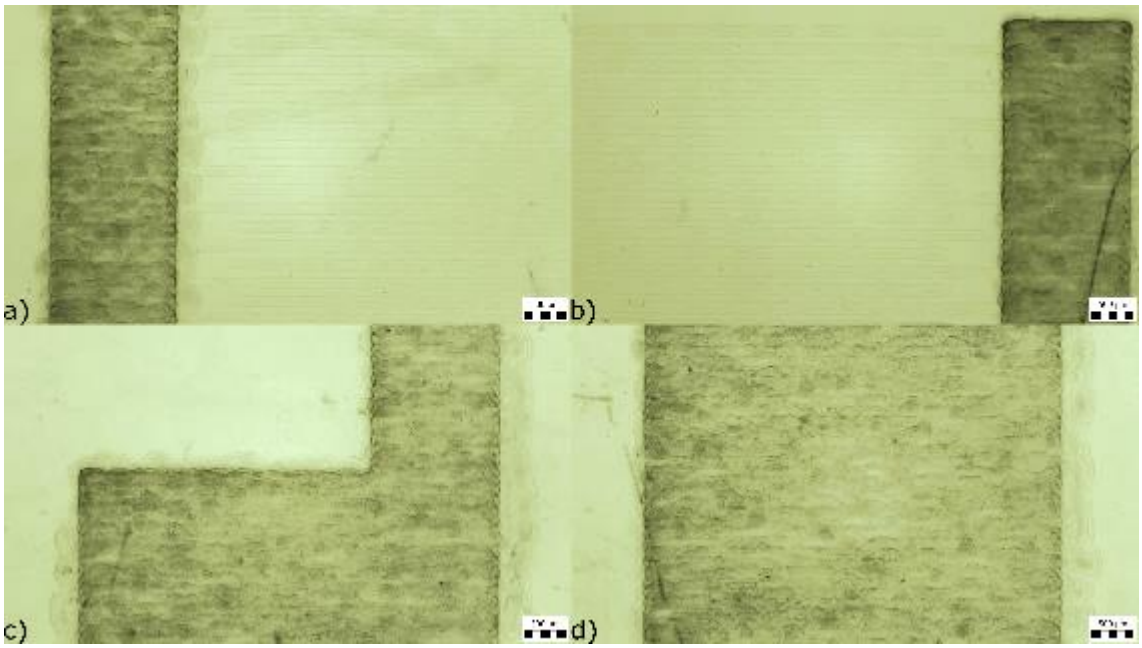

Figure 41. *Sensor pictures taken with a microscope.*

In addition, the total thickness of the fabricated sensors was also determined. Figure 42 illustrates the thicknesses of all sensor layers. The thickness of the Parylene-C layers was expected to be 2 µm and 1 µm for the bottom and top layer, respectively. Only PEDOT:PSS electrodes and P(VDF-TrFE) thicknesses were measured individually. The mean value of the PEDOT:PSS layer was around 25 nm. The P(VDF-TrFE) layer thickness was in the range of 1.5 µm to 2.5 µm. The variation between the measured samples might be because of the printing technology used to print the active layer. Screen printing parameters were adjusted manually. Thus, this could have had an impact on the printed layer thickness. Therefore, the total thickness of the sensors was around 6 µm.

Figure 42. *Final samples layers schematic.*

4.4.2 Electrical characterization

Lower capacitance leads to higher voltage sensitivity as discussed in chapter 2.2. Therefore, the capacitance of the final samples was measured. The histogram of the capacitance measurement results is shown in below Figure 43. Capacitance values are in the range of 0.6 pF to 1.4 pF. The average capacitance for the ten samples is 0.99 ± 0.32 pF. Previously, MIM-based flexible piezoelectric sensors, which were fabricated using printed electronics technologies, showed a capacitance value of 1.5 nF [74]. Therefore,

the results indicate that effectively the capacitance of IDE-based sensors is lower than MIM-based sensors and should result in higher sensitivity.

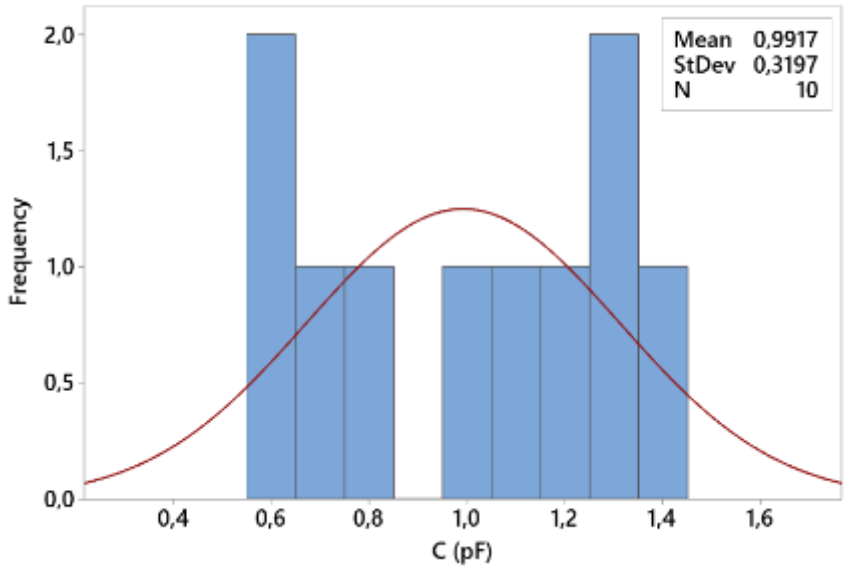

Figure 43. *Histogram of the capacitance of the sensors at 1 kHz.*

Additionally, the capacitance of IDE-based sensors also depends on the distance between fingers. In the previous section, it was shown that the fingers width and finger gap were not uniform. Therefore, this may cause a variation in the capacitance between samples. Computing the capacitance of IDE-based sensors is not as straightforward as for MIM-based sensors; there are more parameters affecting the equivalent capacitance of the IDE-based sensor. Thus, it was not possible to determine an expected capacitance value to compare it with the results. In future, finite element (FE) modeling of the IDE-based sensors should be done to determine an approximate capacitance value.

The high resistance (i.e. low leakage current) of piezoelectric sensors is important for achieving effective poling which is necessary for achieving high sensitivity of the sensor. Resistance was also measured for all the samples. The histogram of the resistance measurement results is shown in Figure 44. It can be seen that the range of the resistance of the samples. Resistance values are in the range of 45 GΩ to 120 GΩ. All the samples were fabricated following the same fabrication process. Thus, the variation on the resistance of the samples could not be influenced by variations on the fabrication processes, such as annealing conditions. However, it can be assumed that the leakage current of the sensors can be neglected owing to their high resistance.

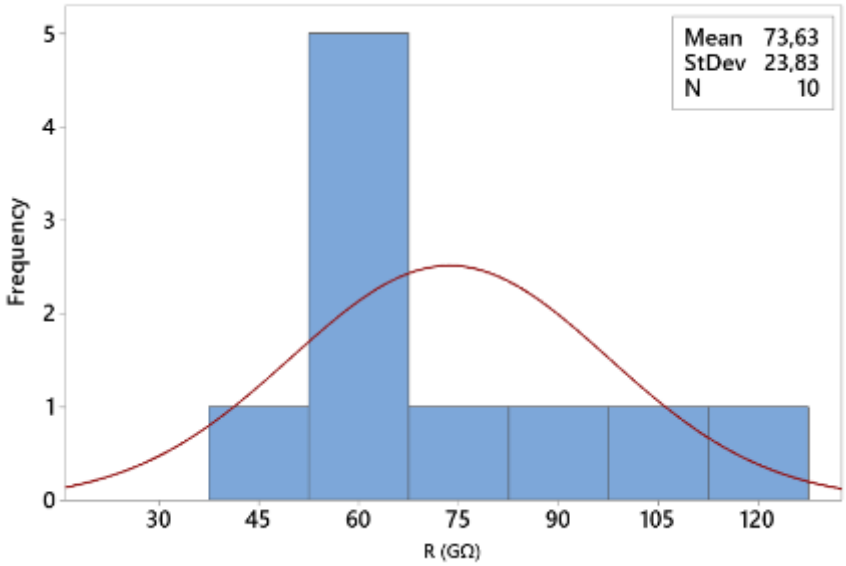

Figure 44. *Histogram of the resistance of the sensors.*

The mean value and coefficient of variation of the capacitance and resistance are listed in Table 13. The coefficient of variation (CV) can be used to examine the variability of measurements in a dataset. The CV value for both cases is high which indicates that the variation between the data points and the mean value is high. This result suggests that there is a high difference in the electrical properties between samples resulting from process variation.

Table 13. *IDE sensor's electrical properties.*

Parameter	Mean	Coefficient of variation (%)
Capacitance @1 kHz	0.99 ± 0.32 pF	32.27
Resistance	73.60 ± 23.83 GΩ	32.36

4.4.3 Sensitivity measurements

In this thesis work, the piezoelectric sensitivity characterization was done to test the piezoelectric response of the samples. However, the normal and bending mode measurements could be affected by different piezoelectric charge coefficients. Therefore, the obtained results not only correspond to the d_{31} or the d_{33} piezoelectric charge coefficient.

The piezoelectric sensitivity measurements of the sensors in normal mode are represented in Figure 45. This histogram represents the mean value of ten measurements from each sample with normal distribution fit. The mean piezoelectric sensitivity varies from 0.5 pC/N to 6 pC/N. However, there was not any reference value to compare the obtained results in this mode. Thus, further analysis should be done to determine which piezoelectric coefficients are activated when performing this measurement.

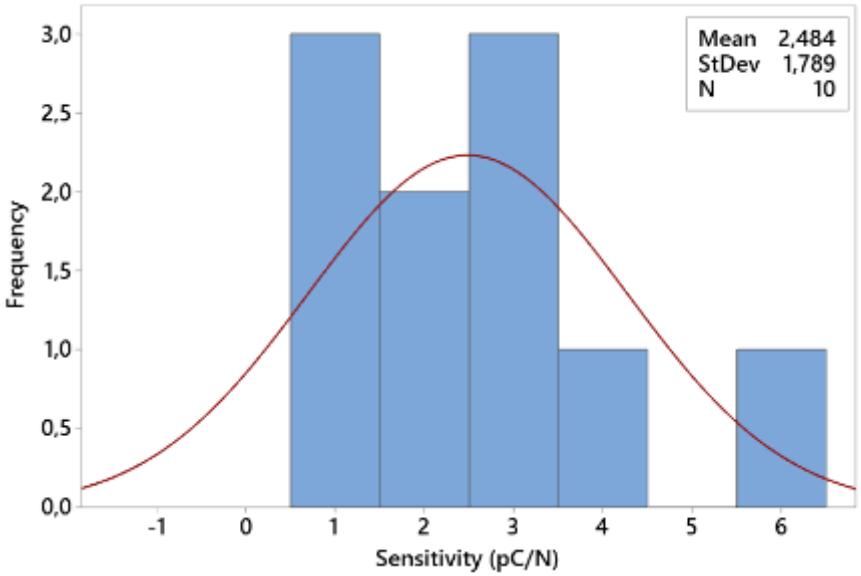

Figure 45. *Histogram of the charge sensitivity measurements in normal mode.*

Additionally, piezoelectric sensitivity was also measured in bending mode. Figure 46 shows the histogram of the piezoelectric sensitivity measurements in this mode. The obtained results are distributed in the range of 1 pC/N to 16 pC/N. Theoretically, IDE-based piezoelectric sensors should show a much higher piezoelectric sensitivity in bending mode than in normal mode. However, the results of the piezoelectric sensitivity characterization did not show a big difference between the examined cases.

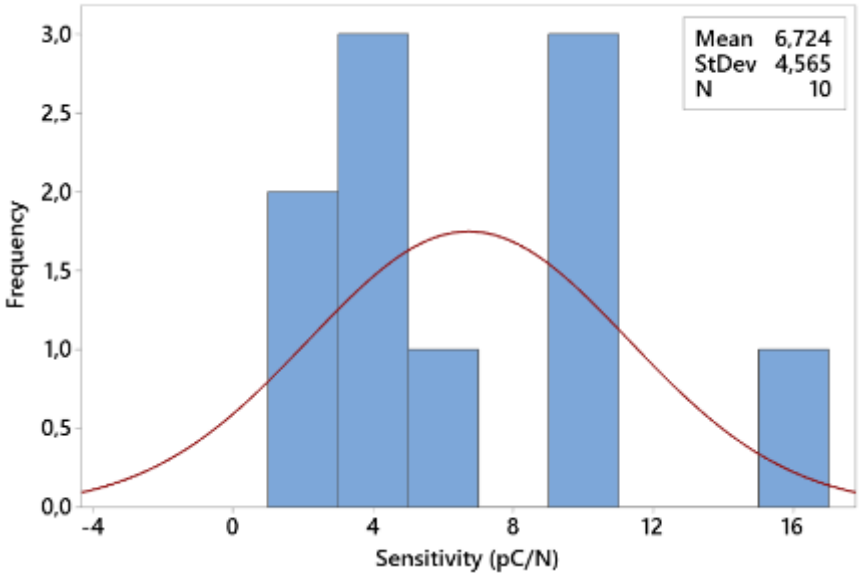

Figure 46. *Histogram of the charge sensitivity measurements in bending mode.*

Therefore, the two-sample T-test was performed to determine if it could be concluded that the measurements represented different piezoelectric modes. The results of the analysis are listed in Table 14. The difference between the means is 4.24, and the P-

values is less than 0.05. Therefore, based on the obtained results, it could be concluded that the examined modes are different.

Table 14. *Two-sample T-test results of piezoelectric sensitivity measurements.*

Population A	Population B	Difference	95% CI for Difference	P-value
Normal	Bending	-4.24	(-7.65; -0.83)	0.019

Furthermore, the generated charge by the applied stress could be vanished by charges present in the environment (i.e. air-borne charges), leakage current (i.e. non-zero conductivity of the dielectric), or by the input resistance of the signal acquisition equipment [75]. Nevertheless, the measurements done in this research were not affected by these conditions. The PEDOT:PSS electrodes were covered with P(VDF-TrFE) which should prevent vanishing of the charges; the resistance of the samples was very high which eliminates the possibility of having a high leakage current. Additionally, the charge generated by the sensors was measured using a charge amplifier. Thus, using this configuration, the measured charge is not affected by the input impedance of the signal acquisition equipment.

4.4.4 Voltage response estimation

Voltage response estimation was calculated based on the charge sensitivity and the capacitance measurements using equation (12). The voltage approximation was calculated for normal and bending mode. Although sensors capacitance was not measured in bending mode, an approximation of the voltage response for this mode was also calculated based on the capacitance measured in normal mode. The capacitance value may be different when the sensors are bent. Figure 47 shows a boxplot of the estimated output voltage for normal and bending mode.

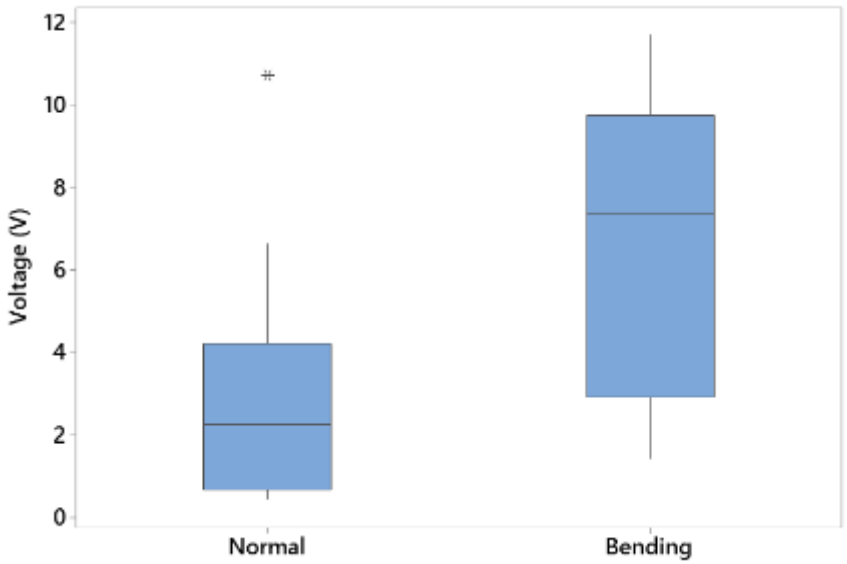

Figure 47. *Boxplot of the estimated output voltage in normal and bending mode.*

It should be noted that it is expected to obtain a much higher output voltage when sensors are operating in bending mode [48]. Thus, statistical analysis was done to examine the obtained results. Some characteristic parameters are listed in Table 15. The difference between the standard deviation and the maximum voltage value of both modes do not show a big difference. Thus, Two-sample T-test was also performed to check if it can be assumed that the data sets were independent of each other. Table 16 lists the results of this test. As the P-value is less than 0.05, it could be concluded that there is a difference between the analyzed modes. Nevertheless, the characterization of the sensors voltage response should be done to analyze the relation between the voltage response and the generated charge.

Table 15. *Statistic values of estimated output voltage*

Voltage	Mean (V)	STD (V)	Min. (V)	Max. (V)
Normal	3.10	3.23	0.44	10.72
Bending	6.84	3.63	1.43	11.68

Table 16. *Two-sample T-test results of output voltage modes.*

Population A	Population B	Difference	95% CI for Difference	P-value
Normal	Bending	-3.74	(-6.98; -0.50)	0.026

4.5 Verification of the sensitivity measurements results

As the characterization of the piezoelectric sensitivity showed inconsistent results, it was decided to verify the piezoelectric sensitivity measurement results. Therefore, the piezoelectric sensitivity was measured from a non-poled sample in normal mode. The motivation was to compare the piezoelectric sensitivity response between a non-poled and a poled sample. However, the obtained results were comparable to those obtained from the poled samples.

Therefore, to detect possible measurement errors, it was measured the piezoelectric sensitivity response before printing the piezoelectric material layer. A set of four samples were measured in normal mode. Each sample was measured in ten different places. The measurement results (sample E1 to E4) are represented in the interval plot shown in Figure 48. The piezoelectric sensitivity in normal mode of the ten poled samples is also represented in this figure (samples S1 to S10). The mean value of the samples without the piezoelectric layer is 0.66 pC/N and the mean of the poled samples is 2.48 pC/N. As can be seen in the figure, there is a difference in the distribution of the obtained results between the two analyzed cases. The piezoelectric sensitivity of the samples E1, E2, E3 and E4 are distributed in the same range and do not show a significant difference between them. However, the piezoelectric sensitivity of samples S1, S6 and S7 are in the same range as the samples without the piezoelectric layer. The low piezoelectric response of these samples could be a result of possible sensor failures. However, it was not possible to determine the reason for the low response since the results in the electrical characterization of these samples did not show a big difference compared to the other samples (see Figure 43 and Figure 44). Thus, these measurements could not be excluded from the analysis.

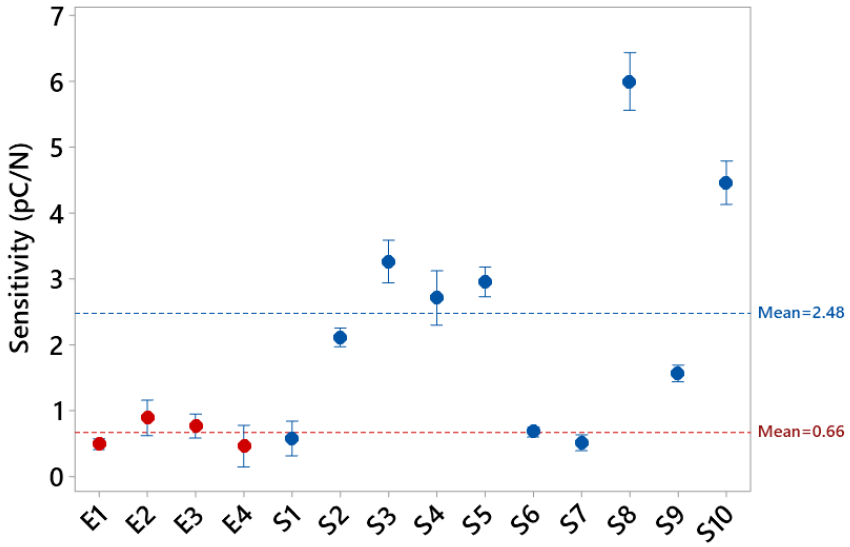

Figure 48. *Interval plot sensitivity measurements in normal mode. Red dots represent the samples without the active layer (Mean = 0.66 pC/N). Blue dots represent the poled samples (Mean = 2.48 pC/N).*

Furthermore, the 1-Sample T test was performed to compare the mean value of the samples without the piezoelectric layer to the poled samples and to determine if there was a statistically significant difference between the two analyzed cases. To perform this test, the mean value of the piezoelectric response of the poled samples in normal mode was used as reference mean (i.e. 2.48 pC/N). Thus, this test determines if the mean of the dataset E1, E2, E3 and E4 is different from the reference mean. The test results are summarized in Table 17. The mean value and the standard deviation of the dataset is listed in this table. In addition, the confidence interval indicates that the mean can be between 0.5420 and 0.7718. The P-value is less than 0.05 which determines that the population mean is different from the poled samples mean in normal mode. Therefore, polarized samples clearly showed some piezoelectric response.

Table 17. *1-Sample T test. Reference mean value = 2.48 pC/N.*

Number of data points	Mean	STD	95% CI for mean	P-value
40	0.6569	0.3593	(0.5420; 0.7718)	0.000

Based on the obtained results, it can be concluded that the piezoelectric response showed by the sensors was not as strong as expected. Furthermore, the variation of the piezoelectric sensitivity between poled samples showed that the piezoelectric properties

are less pronounced in some samples despite the fact that the poling process was performed under the same conditions for all the samples. Therefore, further research have to be done to determine possible sensor failures.

In addition, the piezoelectric sensitivity response of the sensors depends on the piezoelectric properties of the P(VDF-TrFE) layer. Thus, the piezoelectric layer should have been poled properly to show good piezoelectric response. Therefore, based on the obtained results, it can be assumed that the poling process did not fully activate the piezoelectric properties of the P(VDF-TrFE) layer. The poling process could have been limited because of the non-uniform distance between fingers. In addition, it should be pointed out that the electric field does not distribute uniformly during poling. This results in a disparity in the piezoelectric properties of the poled material [76]. There are three different regions between each pair of finger electrodes: an active region, an ineffective region, and a transition region [77]. In the active region, which is formed between the electrodes, the electric field is distributed uniformly. On the contrary, the electric field is not uniform in the ineffective region, which is located above the electrodes. Thus, the electric field is very low in the ineffective region compared to the active region. Furthermore, the transition region is located between the active and the ineffective region. Consequently, it can be assumed that there is a poling loss factor associated with the non-uniformity of the poling process. The poling loss factor also depends on the relation between the electrode finger width and the piezoelectric layer thickness [78]. Thus, further analysis should be done to examine the poling losses, and to determine an optimal finger width and piezoelectric layer thickness.

Additionally, the piezoelectric material cannot be properly poled if the electric field is very low. The PEDOT:PSS printed patterns showed a very high resistance, which results in conductor losses. As a consequence, the applied electric field could have not been as high as required because of the conductor losses. Therefore, the conductivity of the electrodes has to be improved to eliminate possible losses associated with the poor conductivity.

5. CONCLUSIONS

Flexible pressure sensors have the potential to be used in healthcare monitoring applications and artificial intelligence systems. In this thesis, the design and fabrication of ultra-thin IDE flexible pressure sensors were evaluated. The transduction method used in this sensor was piezoelectricity. The sensor was fabricated using printing technologies. The IDE structure was inkjet printed while the active layer was fabricated using screen-printing. It was demonstrated that printing technologies are compatible to fabricate these types of flexible electronic devices. In addition, a set of sensors was fabricated to characterize their electrical and piezoelectric properties by measuring their resistance, capacitance, and piezoelectric sensitivity. An analysis of the characterization results was done to evaluate the performance of the samples.

The sensor substrate selected was Parylene-C. This material showed high mechanical stability after all the fabrication processes. However, it was necessary to apply a surface treatment to the Parylene-C layer before printing the conductive material. This process was done to change the material from hydrophobic to hydrophilic. It was found that UV/O_3 could be employed to change the surface properties of Parylene-C. Therefore, the next test was to analyze the effect of UV/O_3 treatment exposure time on printed patterns. Droplet size variation and line width variation was analyzed when the substrate had been treated. Based on the results of this test, it was found that it was enough to treat the material for 10 minutes to print uniform patterns. Furthermore, the results of the line width test were used to find the optimal drop spacing to print the IDE structure.

The conductive material used for the fabrication of the IDE structure was a commercial PEDOT:PSS ink. The ink conductivity was evaluated before the fabrication of the IDE patterns. The objective of this test was to examine the conductivity of the lines that would be used in the IDE structure. However, the characterization results showed that the printed lines exhibited poor conductivity. Furthermore, the surface profile of the printed lines was measured, and it was observed that the distribution of the material was dominated by the coffee ring effect. The average thickness of the printed lines was much lower than the manufacturer recommendations. Therefore, the non-uniformity and low thickness of the printed lines had an impact on the material conductivity.

The fabrication of the sensor was fully done using printing technologies. Inkjet printing was a suitable method to print the electrodes structure. Nevertheless, the measured pattern dimensions showed variations on the IDE fingers width and gap between fingers.

Non-uniform finger width and therefore non-uniform finger gap could be decreased by optimizing the electrodes fabrication process. In addition, the piezoelectric material was screen-printed. Printing the active material on top of the inkjet printed electrodes did not show any major inconvenience. Thus, the combination of both technologies to fabricate this type of sensor was successful.

The electrical properties of the sensor samples were also analyzed. It was demonstrated that IDE-based sensors can show a lower capacitance value compared to MIM-based devices. In addition, the piezoelectric sensitivity of the samples was evaluated. Sensitivity measurements were done in two modes, without bending and by bending a small area of the samples. Despite the weak piezoelectric response, the piezoelectric characterization results are promising and further research have to be done in order to fully activate the piezoelectric properties of the piezoelectric material used in this study.

In future, how to improve the piezoelectric sensitivity of the samples should be further studied. Thus, it is necessary to enhance the conductivity of the electrodes. To increase the conductivity of the electrodes, it could be possible to examine how to print thicker lines without increasing the line width. In addition, an alternative to overcome the poor conductivity issue is to use a more conductive ink. For example, the IDE structure could be printed using a high conductive PEDOT:PSS ink (e.g. conductivity of 700S/cm) or nano-silver ink. This will eliminate the conductor losses because of the poor conductivity and will guarantee that the applied electric field during the poling process is high enough.

In addition, modeling of the IDE-based sensors could be done to optimize the IDE dimensions. This could also help to examine the impact of the IDE dimensions on the poling losses because of the non-uniform electric field distribution. Thus, based on this analysis, it could be studied if changes in the current IDE structure dimensions should be done. Furthermore, according to the literature, it is necessary to use an optimal piezoelectric layer thickness to guarantee that the poling field penetrates all the piezoelectric material layer. Thus, this could be also found by modeling the sensors. Moreover, modeling could also be used to analyze the impact of the sensor dimensions on the electrical properties of the sensors.

Additionally, sensor electrodes could be optimized to decrease the areas where the poling electric field is non-uniform. For instance, a second IDE structure could be printed on top of the P(VDF-TrFE) layer, and it should be aligned to the IDE structure under the P(VDF-TrFE) layer. Thus, the area, where the dipoles have been oriented during the poling process, will increase. Alternatively, the sensor electrodes structure could be fabricated using a 3D IDE approach. This could be done by increasing the thickness of the

electrode fingers. Thus, the contact area between the fingers and the piezoelectric material will increase, and the area where the poling electric field is uniform will also increase. Printing multiple layers could be used to fabricate 3D interdigitated electrodes.

In conclusion, ultra-thin IDE sensors were fabricated using printed electronics technologies. Additionally, the low thickness of the fabricated sensors (i.e. < 10 µm) could allow to attach them to the human skin without using adhesive patches. Nevertheless, further research has to be done to enhance the piezoelectric properties of the sensors and consequently be able to use them to measure the human pulse wave signal.

REFERENCES

[1] D. Dias and J. P. S. Cunha, “Wearable health devices—vital sign monitoring, systems and technologies,” *Sensors (Switzerland)*, vol. 18, no. 8, p. 2414, Jul. 2018.

[2] Y. Wang *et al.*, “Low-cost, μm-thick, tape-free electronic tattoo sensors with minimized motion and sweat artifacts,” *npj Flex. Electron.*, vol. 2, no. 1, p. 6, 2018.

[3] Y. R. Jeong, G. Lee, H. Park, and J. S. Ha, “Stretchable, Skin-Attachable Electronics with Integrated Energy Storage Devices for Biosignal Monitoring,” *Acc. Chem. Res.*, vol. 52, no. 1, pp. 91–99, Jan. 2019.

[4] S. Choi, H. Lee, R. Ghaffari, T. Hyeon, and D. H. Kim, “Recent Advances in Flexible and Stretchable Bio-Electronic Devices Integrated with Nanomaterials,” *Adv. Mater.*, vol. 28, no. 22, pp. 4203–4218, 2016.

[5] Y. Khan, A. E. Ostfeld, C. M. Lochner, A. Pierre, and A. C. Arias, “Monitoring of Vital Signs with Flexible and Wearable Medical Devices,” *Adv. Mater.*, vol. 28, no. 22, pp. 4373–4395, Jun. 2016.

[6] Y. Liu, M. Pharr, and G. A. Salvatore, “Lab-on-Skin: A Review of Flexible and Stretchable Electronics for Wearable Health Monitoring,” *ACS Nano*, vol. 11, no. 10, pp. 9614–9635, Oct. 2017.

[7] J. C. Yang, J. Mun, S. Y. Kwon, S. Park, Z. Bao, and S. Park, “Electronic Skin: Recent Progress and Future Prospects for Skin-Attachable Devices for Health Monitoring, Robotics, and Prosthetics,” *Adv. Mater.*, vol. 0, no. 0, p. 1904765, Sep. 2019.

[8] D. Y. Park *et al.*, “Self-Powered Real-Time Arterial Pulse Monitoring Using Ultrathin Epidermal Piezoelectric Sensors,” *Adv. Mater.*, vol. 29, no. 37, p. 1702308, Oct. 2017.

[9] T. Sekine *et al.*, “Fully Printed Wearable Vital Sensor for Human Pulse Rate Monitoring using Ferroelectric Polymer,” *Sci. Rep.*, vol. 8, no. 1, p. 4442, 2018.

[10] D. Thuau, K. Kallitsis, F. D. Dos Santos, and G. Hadziioannou, “All inkjet-printed piezoelectric electronic devices: Energy generators, sensors and actuators,” *J. Mater. Chem. C*, vol. 5, no. 38, pp. 9963–9966, 2017.

[11] S. H. Park, H. B. Lee, S. M. Yeon, J. Park, and N. K. Lee, “Flexible and Stretchable Piezoelectric Sensor with Thickness-Tunable Configuration of Electrospun Nanofiber Mat and Elastomeric Substrates,” *ACS Appl. Mater. Interfaces*, vol. 8, no. 37, pp. 24773–24781, Sep. 2016.

[12] M. M. Laurila *et al.*, “A fully printed ultra-thin charge amplifier for on-skin biosignal measurements,” *IEEE J. Electron Devices Soc.*, vol. 7, pp. 566–574, 2019.

[13] F. A. Viola, A. Spanu, P. C. Ricci, A. Bonfiglio, and P. Cosseddu, “Ultrathin, flexible and multimodal tactile sensors based on organic field-effect transistors,” *Sci. Rep.*, vol. 8, no. 1, Dec. 2018.

[14] S. Khan, W. Dang, L. Lorenzelli, and R. Dahiya, “Flexible Pressure Sensors Based on Screen-Printed P(VDF-TrFE) and P(VDF-TrFE)/MWCNTs,” *IEEE Trans. Semicond. Manuf.*, vol. 28, no. 4, pp. 486–493, 2015.

[15] J. Byun *et al.*, “Fully printable, strain-engineered electronic wrap for customizable soft electronics,” *Sci. Rep.*, vol. 7, p. 45328, Mar. 2017.

[16] M. T. Chorsi *et al.*, “Piezoelectric Biomaterials for Sensors and Actuators,” *Adv. Mater.*, vol. 31, no. 1, p. 1802084, Jan. 2019.

[17] W. Heywang, K. Lubitz, and W. Wersing, *Piezoelectricity: Evolution and Future of a Technology, 1st edition*. Springer Berlin Heidelberg, 2008.

[18] J. Tichý, J. Erhart, E. Kittinger, and J. Prívratská, *Fundamentals of Piezoelectric Sensorics: Mechanical, Dielectric, and Thermodynamical Properties of Piezoelectric Materials*. Springer Berlin Heidelberg, 2010.

[19] M. S. Vijaya, *Piezoelectric Materials and Devices: Applications in Engineering and Medical Sciences*. CRC Press, 2016.

[20] T. Furukawa, “Piezoelectricity and Pyroelectricity in Polymers,” *IEEE Trans. Electr. Insul.*, vol. 24, no. 3, pp. 375–394, 1989.

[21] H. S. Nalwa and S. Miyata, *Nonlinear Optics of Organic Molecules and Polymers*. Taylor & Francis, 1996.

[22] S. Banerjee, W. Du, U. Sundar, and K. A. Cook-Chennault, “Piezoelectric and dielectric characterization of mwcnt-based nanocomposite flexible films,” *J. Nanomater.*, vol. 2018, pp. 1–15, Sep. 2018.

[23] R. G. Driggers, *Encyclopedia of Optical Engineering: Pho-Z, pages 2093-2111*. Marcel Dekker, 2003.

[24] H. Li, C. Tian, and Z. D. Deng, “Energy harvesting from low frequency applications using piezoelectric materials,” *Appl. Phys. Rev.*, vol. 1, no. 4, p. 41301, Nov. 2014.

[25] X. Wang, Z. Liu, and T. Zhang, “Flexible Sensing Electronics for Wearable/Attachable Health Monitoring,” *Small*, vol. 13, no. 25, p. 1602790, Jul. 2017.

[26] F. Xu *et al.*, “Recent developments for flexible pressure sensors: A review,” *Micromachines*, vol. 9, no. 11, p. 580, Nov. 2018.

[27] Y. Zang, F. Zhang, C. A. Di, and D. Zhu, “Advances of flexible pressure sensors toward artificial intelligence and health care applications,” *Mater. Horizons*, vol. 2, no. 2, pp. 140–156, 2015.

[28] M. D. Maeder, D. Damjanovic, and N. Setter, “Lead free piezoelectric materials,” *J. Electroceramics*, vol. 13, no. 1–3, pp. 385–392, 2004.

[29] M. Chen-Glasser, P. Li, J. Ryu, and S. Hong, “Piezoelectric Materials for Medical Applications,” in *Piezoelectricity - Organic and Inorganic Materials and Applications*, 2018.

[30] PiezoTech Arkema, “TDS PIEZOTECH® FC INK P For Printed Organic Electronics, Smart Textiles and Plastronics.” 2018.

[31] V. Bharti, T. Kaura, and R. Nath, “Ferroelectric hysteresis in simultaneously stretched and corona-poled PVDF films,” *IEEE Trans. Dielectr. Electr. Insul.*, vol. 4, no. 6, pp. 738–741, 1997.

[32] Y. Q. Fu *et al.*, “Advances in piezoelectric thin films for acoustic biosensors, acoustofluidics and lab-on-chip applications,” *Prog. Mater. Sci.*, vol. 89, pp. 31–91, 2017.

[33] Y. Zhang, T. Nayak, H. Hong, and W. Cai, “Biomedical Applications of Zinc Oxide Nanomaterials,” *Curr. Mol. Med.*, vol. 13, no. 10, pp. 1633–1645, Dec. 2013.

[34] O. A. Azeez, R. S. Sabry, M. A. M. Hassan, and S. F. Madlul, “Synthesis and characteristics of screen printed ZnO thick films nanostructures grown using different methods,” *J. Mater. Sci. Mater. Electron.*, vol. 26, no. 6, pp. 4051–4061, 2015.

[35] S. K. Dey, K. D. Budd, and D. A. Payne, “Thin-film ferroelectrics of PZT of sol-gel processing,” *IEEE Trans. Ultrason. Ferroelectr. Freq. Control*, vol. 35, no. 1, pp. 80–81, 1988.

[36] J. Lyu, I. Fina, R. Solanas, J. Fontcuberta, and F. Sánchez, “Tailoring Lattice Strain and Ferroelectric Polarization of Epitaxial BaTiO3 Thin Films on Si(001),” *Sci. Rep.*, vol. 8, no. 1, p. 495, 2018.

[37] B. D. Stojanovic, C. R. Foschini, V. Z. Pejovic, V. B. Pavlovic, and J. A. Varela, “Electrical properties of screen printed BaTiO3 thick films,” *J. Eur. Ceram. Soc.*, vol. 24, no. 6, pp. 1467–1471, 2004.

[38] T. Futakuchi and K. Tanino, “Preparation of PbTiO3 thin films by screen printing method,” *Jpn. J. Appl. Phys.*, vol. 33, no. 12R, pp. 662–669, 1994.

[39] Y. Yan, J. E. Zhou, D. Maurya, Y. U. Wang, and S. Priya, “Giant piezoelectric voltage coefficient in grain-oriented modified PbTiO 3 material,” *Nat. Commun.*, vol. 7, no. 1, p. 13089, 2016.

[40] N. Meng, X. Zhu, R. Mao, M. J. Reece, and E. Bilotti, “Nanoscale interfacial electroactivity in PVDF/PVDF-TrFE blended films with enhanced dielectric and ferroelectric properties,” *J. Mater. Chem. C*, vol. 5, no. 13, pp. 3296–3305, Jan. 2017.

[41] J. S. Harrison and Z. Ounaies, “Polymers, Piezoelectric,” *Encyclopedia of Smart Materials*. 15-Jul-2002.

[42] N. Jia, Q. He, J. Sun, G. Xia, and R. Song, “Crystallization behavior and electroactive properties of PVDF, P(VDF-TrFE) and their blend films,” *Polym. Test.*, vol. 57, pp. 302–306, 2017.

[43] K. El-Hami, A. Ribbe, S. Isoda, and K. Matsushige, “Structural analysis of the P(VDF/TrFE) copolymer film,” *Chem. Eng. Sci.*, vol. 58, no. 2, pp. 397–400, 2003.

[44] A. Bongrain *et al.*, “A new technology of ultrathin AlN piezoelectric sensor for pulse wave measurement,” *Procedia Eng.*, vol. 120, pp. 459–463, Dec. 2015.

[45] C. Lü, S. Wu, B. Lu, Y. Zhang, Y. Du, and X. Feng, “Ultrathin flexible piezoelectric sensors for monitoring eye fatigue,” *J. Micromechanics Microengineering*, vol. 28, no. 2, Dec. 2018.

[46] L. Persano *et al.*, “High performance piezoelectric devices based on aligned arrays of nanofibers of poly(vinylidenefluoride-co-trifluoroethylene),” *Nat. Commun.*, vol. 4, p. 1633, Mar. 2013.

[47] T. Q. Trung and N. E. Lee, “Flexible and Stretchable Physical Sensor Integrated Platforms for Wearable Human-Activity Monitoringand Personal Healthcare,” *Adv. Mater.*, vol. 28, no. 22, pp. 4338–4372, Jun. 2016.

[48] K. Il Park *et al.*, “Highly-efficient, flexible piezoelectric PZT thin film nanogenerator on plastic substrates,” *Adv. Mater.*, vol. 26, no. 16, pp. 2514–2520, Apr. 2014.

[49] S. B. Kim, H. Park, S. H. Kim, H. C. Wikle, J. H. Park, and D. J. Kim, “Comparison of MEMS PZT cantilevers based on d31 and d 33 modes for vibration energy harvesting,” *J. Microelectromechanical Syst.*, vol. 22, no. 1, pp. 26–33, Feb. 2013.

[50] K. J. Latimer, J. W. Evans, M. A. Cowell, and P. K. Wright, “Modeling of interdigitated electrodes and supercapacitors with porous interdigitated electrodes,” *J. Electrochem. Soc.*, vol. 164, no. 4, pp. A930–A936, Jan. 2017.

[51] P. Van Gerwen *et al.*, “Nanoscaled interdigitated electrode arrays for biochemical sensors,” *Sensors Actuators, B Chem.*, vol. 49, no. 1–2, pp. 73–80, 1998.

[52] J. C. Park, J. Y. Park, and Y. P. Lee, “Modeling and characterization of piezoelectric d33-Mode MEMS energy harvester,” *J. Microelectromechanical Syst.*, vol. 19, no. 5, pp. 1215–1222, Nov. 2010.

[53] E. Cantatore, *Application of Organic and Printed Electronics - A Technology-Enabled Revolution*. Springer US, 2013.

[54] I. M. Hutchings and G. D. Martin, *Inkjet Technology for Digital Fabrication*. Wiley, 2012.

[55] B. Derby, “Inkjet Printing of Functional and Structural Materials: Fluid Property Requirements, Feature Stability, and Resolution,” in *Annual Review of Materials Research*, vol. 40, no. 1, 2010, pp. 395–414.

[56] G. Nisato, D. Lupo, and S. Ganz, Eds., *Organic and Printed Electronics*. Singapore: PAN STANFORD PUBLISHING, 2016.

[57] K. Suganuma, *Introduction to Printed Electronics*, vol. 74. Springer New York, 2014.

[58] J. Ortigoza-Diaz *et al.*, “Techniques and Considerations in the Microfabrication of Parylene C Microelectromechanical Systems,” *Micromachines*, vol. 9, p. 422, Aug. 2018.

[59] B. J. Kim and E. Meng, “Micromachining of Parylene C for bioMEMS,” *Polym. Adv. Technol.*, vol. 27, no. 5, pp. 564–576, Jan. 2016.

[60] C. L. Chen, E. Lopez, Y. J. Jung, S. Müftü, S. Selvarasah, and M. R. Dokmeci, “Mechanical and electrical evaluation of parylene- C encapsulated carbon nanotube networks on a flexible substrate,” *Appl. Phys. Lett.*, vol. 93, no. 9, p. 93109, Sep. 2008.

[61] K. Sun *et al.*, “Review on application of PEDOTs and PEDOT:PSS in energy conversion and storage devices,” *J. Mater. Sci. Mater. Electron.*, vol. 26, no. 7,

pp. 4438–4462, Jul. 2015.

[62] Heraeus, *Inspection Certificate 3.1 per EN 10204*. .

[63] T. Y. Lin, T. T. Pfeiffer, and P. B. Lillehoj, “Stability of UV/ozone-treated thermoplastics under different storage conditions for microfluidic analytical devices,” *RSC Adv.*, vol. 7, no. 59, pp. 37374–37379, 2017.

[64] S. Rajala, M. Schouten, G. Krijnen, and S. Tuukkanen, “High Bending-Mode Sensitivity of Printed Piezoelectric Poly(vinylidenefluoride- co-trifluoroethylene) Sensors,” *ACS Omega*, vol. 3, no. 7, pp. 8067–8073, Jul. 2018.

[65] M. L. Sham, J. Li, P. C. Ma, and J. K. Kim, “Cleaning and functionalization of polymer surfaces and nanoscale carbon fillers by uv/ozone treatment: A review,” *J. Compos. Mater.*, vol. 43, no. 14, pp. 1537–1564, Jun. 2009.

[66] Y. Yuan and T. R. Lee, “Contact angle and wetting properties,” in *Springer Series in Surface Sciences*, vol. 51, no. 1, G. Bracco and B. Holst, Eds. Berlin, Heidelberg: Springer Berlin Heidelberg, 2013, pp. 3–34.

[67] T. Trantidou, T. Prodromakis, and C. Toumazou, “Oxygen plasma induced hydrophilicity of Parylene-C thin films,” *Appl. Surf. Sci.*, vol. 261, pp. 43–51, 2012.

[68] X. P. Bi, N. L. Ward, B. P. Crum, and W. Li, “Plasma-treated switchable wettability of parylene-C surface,” in *2012 7th IEEE International Conference on Nano/Micro Engineered and Molecular Systems, NEMS 2012*, 2012, pp. 222–225.

[69] M. Vakilian and B. Y. Majlis, *Study of interdigitated electrode sensor for lab-on-chip applications*. 2014.

[70] D. Soltman and V. Subramanian, “Inkjet-printed line morphologies and temperature control of the coffee ring effect,” *Langmuir*, vol. 24, no. 5, pp. 2224–2231, Mar. 2008.

[71] Minitab, “Overview for 2-Sample t.” [Online]. Available: https://support.minitab.com/en-us/minitab-express/1/help-and-how-to/basic-statistics/inference/how-to/two-samples/2-sample-t/interpret-the-results/key-results/. [Accessed: 10-Oct-2019].

[72] F. Ely *et al.*, “Patterning quality control of inkjet printed PEDOT:PSS films by wetting properties,” *Synth. Met.*, vol. 161, no. 19–20, pp. 2129–2134, 2011.

[73] M. Nogi, H. Koga, and K. Suganuma, “Highly conductive ink-jet-printed lines,” in *Organic Electronics Materials and Devices*, S. Ogawa, Ed. Tokyo: Springer Japan, 2015, pp. 117–137.

[74] M. Laurila *et al.*, “Evaluation of printed P(VDF-TrFE) pressure sensor signal quality in arterial pulse wave measurement,” *IEEE Sens. J.*, p. 1, 2019.

[75] P. P. L. Regtien, *Sensors for Mechatronics*. 2012.

[76] R. Paradies and M. M. Melnykowycz, “State of stress in piezoelectric elements with interdigitated electrodes,” *J. Electroceramics*, vol. 24, no. 3, pp. 137–144, 2010.

[77] W. Beckert and W. S. Kreher, “Modelling piezoelectric modules with interdigitated

electrode structures," *Comput. Mater. Sci.*, vol. 26, no. SUPPL., pp. 36–45, 2003.

[78] R. R. Knight, C. Mo, and W. W. Clark, "MEMS interdigitated electrode pattern optimization for a unimorph piezoelectric beam," *J. Electroceramics*, vol. 26, no. 1–4, pp. 14–22, 2011.